LainePoiss™— a lightweight and ice-resistant wave buoy

Victor Alari*

Tallinn University of Technology, Department of Marine Systems, Akadeemia tee 15a, 12611, Tallinn, Estonia.

Jan-Victor Björkqvist

Tallinn University of Technology, Department of Marine Systems, Akadeemia tee 15a, 12611, Tallinn, Estonia, and Finnish Meteorological Institute, Marine Research, Erik Palménin aukio 1, P.O. Box 503, FI-00101 Helsinki, Finland.

Valdur Kaldvee, Kristjan Mölder

WiseParker OÜ, Pärna 3, 10128, Tallinn, Estonia.

Sander Rikka

Tallinn University of Technology, Department of Marine Systems, Akadeemia tee 15a, 12611, Tallinn, Estonia.

Anne Kask-Korb

Tallinn University of Technology, Estonian Maritime Academy, Kopli 101, 11712 Tallinn, Estonia.

Kaimo Vahter, Siim Pärt, Nikon Vidjajev

Tallinn University of Technology, Department of Marine Systems, Akadeemia tee 15a, 12611, Tallinn, Estonia.

19 Hannes Tõnisson

20 *Tallinn University, Institute of Ecology, Uus Sadama 5, 10120 Tallinn, Estonia.*

21 **Corresponding author*: Victor Alari, victor.alari@taltech.ee

ABSTRACT

Wave buoys are a popular choice for measuring sea surface waves, and there is also an increasing interest for wave information from ice-covered water bodies. Such measurements require cost-effective, easily deployable, and robust devices. We have developed LainePoiss (LP)—an ice-resistant and lightweight wave buoy. It calculates the surface elevation by double integrating the data from the inertial sensors of the micro-electromechanical system (MEMS), and transmits wave parameters and spectra in real-time over cellular or satellite networks. LP was validated through: 1) sensor tests, 2) wave tank experiments, 3) a field validation against a Directional Waverider, 4) an inter-comparison of several buoys in the field, and 5) field measurements in the Baltic Sea marginal ice zone. These extensive field and laboratory tests confirmed that LP performed well (e.g., the bias of H_{m_0} in the field was 0.01 m, correlation 0.99 and scatter index of 8 %). LP was also deployed with an Unmanned Aerial Vehicle and we present our experience of such operations. One issue that requires further development is the presence of low-frequency artefacts caused by the dynamic noise of the gyroscope. For now, a correction method is presented to deal with the noise.

Significance statement. Operational wave buoys are large and therefore expensive and inconvenient to deploy. Many commercially available devices cannot measure short waves and are not tested in ice. Our purpose was to develop an affordable wave buoy that is lightweight, ice-resistant, capable of measuring short waves, and also has a longer operating life than existing research buoys. The buoy is easily deployed with a small boat or even an industrial drone, thus reducing operating costs. The buoy is accurate, and captures waves that are too short for operational wave buoys. This is relevant for coastal planning in e.g., archipelagos and narrow fjords. We measured waves in ice in the Baltic Sea, and are planning to extend these measurements to Antarctica.

1. Introduction

Wind-generated waves dominate the spectrum of ocean surface vertical variance (Munk 1950; Holthuijsen 2007). These waves are observed visually, but an objective quantification of wave heights, lengths, and propagation directions requires measurements with in-situ or remote sensing technologies. This paper focuses on a newly developed wave measuring buoy.

In-situ instruments do not measure wave properties directly. At the sea surface, wave buoys should follow the three-dimensional movement of water particles while measuring the inertial data or the Doppler shift of a GPS signal (Herbers et al. 2012). Below the sea surface, pressure transducers measure wave-induced pressure fluctuations (Cavaleri 1980), Doppler current meters measure the wave-induced orbital motions (Gordon and Lohrmann 2002), and inverted echo-sounders measure acoustic travel time between the device and the sea surface (Wadhams 1978). Wave gauges piercing the sea surface measure the up-and-down movement of water through electrical capacitance or resistance (Donelan et al. 1985; Graber et al. 2000). The surface wave spectra is then calculated from the measured physical quantity by mathematical transformations and wave theory.

All the measurements techniques in the above (non-exhaustive) list are feasible, but have their own limitations and peculiarities. For example, gaps in data due to salty water over washing the buoy and blocking the GPS signal (Björkqvist et al. 2016), spurious data in echo-soundings generated by breaking waves and diminishing of short-waves in pressure recordings (Bishop and Donelan 1987). More generally, the size of the instrument, the basic measurement principle and the met–ocean conditions affect the measurement result. Besides inherent limitations, operational and practical considerations, like ease of use and cost of the instrument, might be important.

Majority of operational wave measurements are done with surface-following buoys, which may also include sensors for recording atmospheric and upper ocean state variables (Thomson 2012). These buoys can be tethered to the sea floor or allowed to drift under the influence of wind and currents. An advantage of these buoys is their long operational life (several years). However, the established operational buoys are large and heavy. The National Data Buoy Center of NOAA has tailored met–ocean buoys, equipped with wave measuring sensors, ranging from 1.8 m to 12 m in diameter. The widely used Datawell Waverider Mk-III, TRIAXYS Directional Wave Buoy and Fugro Seawatch Mini II Buoy have diameters of at least 70 cm and weights of over 100 kg. These off-the-shelf operational buoys may not be an affordable choice for simultaneous deployments, and their handling requires expertise as well as vessel for deployment. These issues are somewhat alleviated with buoys as the Datawell DWR-G4, which weighs 17 kg, has a diameter of 40 cm and a battery life of 30 days.

Recent advances in accurate and low-cost motion sensors and GPS technology have led to the development of a low-cost easy-to-handle wave measurement platform called Spotter (Raghukumar et al. 2019; Lancaster et al. 2021). It is a sea state detector with unprecedented coverage (Smit et al. 2021; Houghton et al. 2021) and thanks to its small size, it might turn out to be a practical tool for estimating wind speed from wave spectra (Voermans et al. 2020). First field experiments

of measuring waves in grease ice with Spotter show promising results in performing these types of observations at a low cost (Kodaira et al. 2020). The simultaneous deployments of several (tens, hundreds) drifting wave buoys is also beneficial for understanding wave–current interaction at coastal and oceanic scales (Pearman et al. 2014; Veras Guimarães et al. 2018) and wave growth in complex archipelagos (Björkqvist et al. 2019) and fjords (Christakos et al. 2021).

In this paper, we describe and validate a new wave buoy called LainePoiss (LP), which uses the micro-electromechanical system (MEMS) inertial measurement unit to detect surface motion. LP was originally designed for wave measurements in ice, but has over 3 years of research and development matured into a valid device; it is already used for real-time wave monitoring in the Baltic Sea. When developing the buoy, we have kept the following combination of performance characteristics in focus: ice-resistant, lightweight, operational, small and affordable. These characteristics allow LP to be used for various research and engineering applications. For example, we are currently planning to use LP for wave measurements in the marginal ice-zone, extending measurement times of operational wave buoys in the seasonally ice covered Baltic Sea, field measurements of shorter-waves in archipelagos and lakes and using Unmanned Aerial Vehicles (UAV) as a rapid method for deployments. LP is also a core infrastructure for validating operational coastal wave models in Estonia.

The structure of the paper is as follows. In Chapter 2, we describe the wave buoy in detail and introduce algorithms for converting the acceleration data into displacement data. In Chapter 3, the omnidirectional and directional wave parameters are defined. Chapter 4 describes different laboratory tests for sensor validation, including standstill measurements of acceleration noise and benchmark tests with monochromatic motions. Thereafter, we will describe the accuracy of the buoy in capturing high-frequency waves in a wave tank. Chapter 5 deals with the field test results. This includes an extensive validation campaign against a Directional Waverider and an

intercomparison of several LP buoys. We also describe drifting experiments results, where an UAV was used as a deployment method. We end Chapter 5 by describing the results of waves-in-ice measurements from the Baltic Sea. In Chapter 6, we discuss the limits and merits of the new technology and conclude our main findings in Chapter 7. Three appendixes end the paper, with the description of the denoising procedure, calculating validation statistics and describing our experience of UAV deployments.

2. Materials and Methods

a. Technical description of the buoy

LP is a spherical wave buoy with a diameter of 32 cm, a height of 22 cm (Fig. 1) and a weight of 3.5 kg. The enclosure is made of two tough glass fiber halves. Between the halves, there is a seal that makes the hull waterproof after it has been bolted together. After the buoy is sealed, it can be turned on and off by holding a magnet to the outside of the hull. Rechargeable lithium-ion batteries, with a capacity of 335 Wh, can power the buoy for roughly two months.

The microcontroller of the buoy is connected to the sensors, the memory and the communication modems through a custom built PCB board (Fig. 2). This controller—using an ARM Cortex-M4 core—was chosen because of its low power consumption, floating point support and digital signal processing functionality.

The inertial sensors of the buoy are a 3D accelerometer, a 3D gyroscope, and a magnetometer. These sensors are part of the Xsens MTi-3 attitude and heading reference system (AHRS). The internal processor of the system synchronizes the sensors, applies calibration models and runs the sensor fusion algorithm. After assembling the buoy, we performed a magnetic calibration that

corrected for the disturbance inflicted to the magnetic field of the Earth by ferromagnetic materials. The device location was logged by a GNSS (Global Navigation Satellite System) receiver.

We configured the output frequency of the inertial data to 50 Hz, and this data is written to an SD-card. Depending on the configuration set by the user, the data is also sent to a cloud server in real time (e.g., every 30 minutes) using cellular LTE or satellite Iridium SBD® networks. The buoy can be configured to use either one or both of these communication options; the buoy always prioritizes the cellular network, but can automatically switch to the satellite network if no cellular coverage exists. We chose the cellular network as the primary communication channel because of its significantly lower data transmission costs. The buoy can therefore also send the raw data through the cellular network, although this option can be disabled to save power.

b. Data processing

The buoy sampled the acceleration with a 50 Hz sampling frequency, and (in the field tests) this data was saved in files containing 65538 measurements (ca 22 minutes). For each deployment, this acceleration data was combined into one long time series from which we constructed 30-minute displacement time series with starting times of :00 and :30 using the following procedure:

1. We constructed 32-minute time series from the continuous acceleration data (:59–:31).

2. The x,y, and z accelerations were low-pass filtered (filter "biting" between 1.28 Hz and 5.12 Hz) with a finite impulse response (FIR) filter that had 162 coefficients before being down-sampled to a 5.12 Hz resolution using a nearest neighbour interpolation. Because of the original 50 Hz sampling frequency, this resulted in a maximum shift on 100 ms of the measurement.

3. The acceleration data was double integrated in Fourier space. Before integration, the white noise was removed for frequencies up to 0.10 Hz, and the amplitudes at the lowest frequencies

were set to zero (see Appendix B for details). We removed 30 seconds from the start and end of the double integrated time series to cut out transient data caused by the Fourier integration.

4. Finally, after accounting for the data lost by FIR-filtering and Fourier integration, we cut the time series to start exactly at :00 or :30 to a 9216 point long block. These 30-minute block coincided exactly with the displacement time series of the Waverider at Suomenlinna, which we used for validation.

The denoising of the acceleration data was performed by estimating the mean amplitude of the Fast Fourier Transform (FFT) of the signal between frequencies 1/100 Hz and 1/30 Hz. The integration was performed in Fourier space, where the removing of the low-frequency energy was applied gradually below 0.05 Hz using a half-cosine function, setting the amplitudes to 0 below 0.04 Hz. This integration procedure is similar to the one used in Rabault et al. (2020). For the field data, a correction to the energy was performed based on the amount of variance that was lost in the denoising. The denoising, compensation and integration procedures are documented in detail in Appendix B.

The 30-minute displacement time series were then used to calculate wave spectra from 100-second blocks using the Welch method with a 50% overlap (35 segments), resulting in a wave spectrum with a 0.01 Hz resolution. Each segment was tapered with a Hann window. The highest frequency used in the spectrum was 1.28 Hz, which corresponds to a 95 cm deep water wavelength and approximately 3 times the buoy diameter. Higher frequencies were starting to be distorted by the size of the buoy when compared to the wave gauge data (see Section 4c on the wave tank experiment).

Note that the data processing procedures in the laboratory experiments differed slightly from the data collected from field tests, since the time series were shorter. Please see Section 4c for details on the exact procedure for laboratory data.

3. Wave parameters

a. Omnidirectional parameters

We used the following definitions of wave parameters. The spectral moments are defined as

$$m_n = \int_{f_0}^{f_1} f^n E(f)\,\mathrm{d}f, \tag{1}$$

where a lower integration frequency of $f_0 = 0.10$ Hz and an upper frequency of $f_1 = 0.58$ Hz was used to match the highest frequency that was reliably captured by the Waverider.

Using the spectral moments we defined the significant wave height:

$$H_{m_0} = 4\sqrt{m_0}. \tag{2}$$

The wave periods were defined as

$$T_{m_{-10}} = \frac{m_{-1}}{m_0} \tag{3}$$

$$T_{m_{01}} = \frac{m_0}{m_1} \tag{4}$$

$$T_{m_{02}} = \sqrt{\frac{m_0}{m_2}} \tag{5}$$

$$T_p = (\operatorname{argmax} E(f))^{-1} \tag{6}$$

$$T_c = \frac{\int_{f_0}^{f_1} f^{-1} E(f)^4\,\mathrm{d}f}{\int_{f_0}^{f_1} E(f)^4\,\mathrm{d}f}. \tag{7}$$

Here, the peak period, T_p, was determined using a parabolic fit. T_c is the so-called characteristic period, which is of the same type that was originally developed as an alternative to peak frequency by Young (1995). Björkqvist et al. (2019) proposed it as a more stable alternative characterisation of a representative wave frequency in archipelago conditions, where the peak period is often ill-defined. Note that we use a slight modification by integrating a weighted average of the inverse of the frequency (f^{-1}) compared to the weighted integration of f by Young (1995) and Björkqvist et al. (2019).

The narrowness of the spectrum was determined by the κ^2-narrowness parameter (Battjes and van Vledder 1984):

$$\kappa^2 = \frac{1}{{m_0}^2}\left(\left[\int_{f_0}^{f_1} E(f)\cos(2\pi f T_{m_{02}})\,\mathrm{d}f\right]^2 + \left[\int_{f_0}^{f_1} E(f)\sin(2\pi f T_{m_{02}})\,\mathrm{d}f\right]^2\right). \tag{8}$$

κ^2 takes values between 1 (infinitely narrow spectrum) and 0 (white noise) and has been found to capture the spectral shape better (especially in the archipelago) than width parameters depending on high moments (m_2 or m_4) (Björkqvist et al. 2019).

b. Directional parameters

Directional parameters were calculated using the first pair of Fourier coefficients, $a_1(f)$ and $b_1(f)$. These coefficients were calculated from the cross-spectra following Longuet-Higgins (1961):

$$a_1(f) = \frac{Q_{ve}(f)}{\sqrt{C_{vv}(f)\,(C_{nn}(f)+C_{ee}(f))}} \tag{9}$$

$$b_1(f) = \frac{Q_{vn}(f)}{\sqrt{C_{vv}(f)\,(C_{nn}(f)+C_{ee}(f))}}, \tag{10}$$

where $Q(f)$ and $C(f)$ are the quadrature- and co-spectra, with subscripts v,e and n referring to the vertical, east and north displacements.

The mean direction at each frequency was calculated as

$$\theta_m(f) = \arctan\left(\frac{a_1(f)}{b_1(f)}\right) + 180, \tag{11}$$

with the mean and peak direction being

$$\theta_m = \arctan\left(\frac{\overline{a_1}}{\overline{b_1}}\right) + 180 \tag{12}$$

$$\theta_p = \theta(f_p) = \arctan\left(\frac{a_1(f_p)}{b_1(f_p)}\right) + 180, \tag{13}$$

where f_p is the peak frequency determined without a parabolic fit.

The directional spread was defined as

$$\sigma(f) = \sqrt{2 - 2m_1^F(f)}, \tag{14}$$

where

$$m_1^F(f) = \sqrt{a_1^2(f) + b_1^2(f)}. \tag{15}$$

The mean and peak spreads were defined as for the directional spread (Eq. 14) using

$$\overline{m}_1^F = \sqrt{\overline{a_1}^2 + \overline{b_1}^2} \tag{16}$$

$$m_1^F(f_p) = \sqrt{a_1^2(f_p) + b_1^2(f_p)}. \tag{17}$$

4. Laboratory tests

a. Sensor static noise

The manufacturer of the MEMS sensor reports a static noise density value of 0.12 $mg(\sqrt{Hz})^{-1}$ for the acceleration sensor. In order to test if this represents the actual noise of a single sensor,

we conducted a standstill measurement, where, at a room temperature of 21°C, we let the sensor measure for 3 hours. We then calculated the power spectrum of the acceleration noise and transformed it to noise displacement spectra by dividing the acceleration spectra with $(2\pi f)^{-4}$. We found that the unused sensor has a higher noise density than the manufacturer's value (Fig. 3). We repeated the same procedure for sensors already used in deployments and found that the noise does not increase with the usage of the sensor (LP1 was used the most, 5100 hours). Therefore, for the sensor noise, we will use the value 0.22 $mg(\sqrt{Hz})^{-1}$. From a practical point of view, this sensor noise level only becomes important when dealing with very low amplitude waves, e.g., waves-in-ice. For the field measurements described in this paper, the static noise of the sensor was subtracted only for the waves-in-ice measurements (Section 5d).

b. Benchmark test

The benchmark tests were conducted with a custom-made device (Fig. 4a). The amplitude was kept constant at 68 mm (+-1 mm), while period was varied between 1 to 25 s by adjusting the speed of the device. Since the device didn't reproduce a perfect sine wave, all the measured acceleration signals had harmonics at multiples of the dominant signal. The measured acceleration signal was transferred to frequency space, the noise was removed and then double integrated and transferred back to time space. Mean amplitudes of N cycles were calculated. N varied between 8 and 30, depending on the cycle period.

The results of the benchmark test for periods 1, 5, 10, 20 and 25 s are shown in Table 1. The sensor is able to measure movement in the wind-wave and swell period range. The difference between the prescribed and measured value depends on the acceleration—the measured amplitude starts to deviate with decreasing acceleration, being 6% at 0.04 Hz.

c. Wave tank

We tested the wave buoy's response to irregular waves in both tethered and free-drift setups. The experiments were conducted in a wave tank (Fig. 4b) owned by the Small Craft Competence Centre of the Tallinn University of Technology. The aim was to validate the high-frequency part of the spectrum and determine the accuracy of LP in conditions which represent wave growth at short fetches.

The 60 m long, 5 m wide and 3 m deep tank uses 6 paddles to generate waves, which are recorded by a capacitance wave height gauge (developed by Akamina Technologies) in the middle of the tank. The duration of wave generation varied from 210 s to 300 s.

For the tests, we moored one buoy 2 m from the wave gauge and let the other two drift. With the JONSWAP spectrum, we made 8 tests (Table 2), in which each combination of peak period and significant wave height was repeated twice. For each test, a 3-minute-long time-series was analyzed. The time series was converted into a displacement power spectra using the Welch method (block length 30 s, 50 % overlap). Neither data sets were decimated; LP data sampled at 50 Hz and wave gauge data sampled at 200 Hz were used.

Significant wave height, integrated between 0.30 Hz and 1.28 Hz, shows a satisfactory match between wave gauge and wave buoys (Table 2). The difference in significant wave height between the buoys and the wave staff was -1–3 cm. The wave spectra (Fig. 5) reveals a similar structure between the wave gauge and buoys up to 1.28 Hz and a slight shift of frequencies of the drifting buoys due to Doppler shift.

5. Field tests

The field tests were conducted in the seasonally ice-covered Baltic Sea, which is an enclosed basin with a maximum fetch of 700 km. The deployments were made within 5 km from the coast (Fig. 6).

a. Comparison against a Directional Waverider

We deployed buoys at two locations close to the operational Directional Waverider DWR-Mk III[1], which was moored at a depth of 20 m outside of Suomenlinna in the Finnish Archipelago (Fig. 6). The measurement area is characterized by tens of islands in varying size and busy recreational and commercial vessel traffic, although the commercial traffic during the deployments was reduced because of COVID-19 restrictions to travel.

With some short gaps, the deployments lasted from June to November 2020 (Table 3). Four different buoys were used, because the battery life of one device did not last for the entire campaign. The buoys were moored approximately 300 m north of the DWR (Fig. 6), where the water depth was 17 m. The recommended mooring consisted of an anchor, a surface float, LP, ropes connecting the assembly, and weights (Fig. 4c). The mooring endured strong winds from all major directions. The maximum 10 minute averages were 15 ms^{-1} (west), 16 ms^{-1} (north), 14 ms^{-1} (east) and 21 ms^{-1} (south), with the gusts reaching 27 ms^{-1}. The buoy was not dragged from its deployment location, which shows that a 25 kg mooring anchor was sufficient.

Two buoys were deployed in June using a small plastic motorboat. In August, one of these buoys was removed and the second one was replaced (using the same boat). In September, the buoy was replaced again using a motorized sailing vessel, and it was finally retrieved with a pilot boat in the beginning of December.

[1]Then owned by the City of Helsinki, now owned by Finnish Meteorological Institute.

The spectra from both LP and DWR were integrated between 0.10–0.58 Hz, and both devices generally agreed on the wave statistics for the field experiment (Table 4; see Appendix A for the definition of the statistical parameters). The mean significant wave height was 0.42 m, which is 0.10 m higher than the 2016–2018 measured average (Björkqvist et al. 2019). Both LP and DWR measured a similar highest significant wave height, with the difference being within the expected sampling variability. The wave periods agreed better the more they were determined by the shorter waves, with T_{m02} showing the best agreement and T_p the worst. The maximum peak period values for LP are probably not realistic but stem from the low-frequency noise dominating the lowest integration frequency when total energy was very low. The dominant wave direction for both instruments was south-southwest. The spreading was, in a mean sense, slightly higher for LP than for DWR.

Overall, the significant wave height measured by LP and DWR matched well (Figs. 7–9), with a 0.01 m bias and 0.99 correlation coefficient (Table 5). During two occasions in the first deployment, LP measured an around 0.2 m higher significant wave height than the DWR (Fig. 7b). Both of these cases took place during around 10 ms^{-1} easterly winds, but LP and DWR matched up well during roughly 13 ms^{-1} easterly winds in the autumn (Fig. 9b). We have not yet determined a definitive reason for the discrepancy during the summer cases. A tangling of the moorings of the LPs is improbable since both LPs measured similar wave heights.

The wave periods determined from spectral moments compared well to those from the DWR (Fig. 10b,d,f). The scatter index was 3–5%, with the biases being no more than 0.16 s (Table 5). The scatter index is highest (23 %) for the peak period (Table 5). The general poor validation for the peak period is explained by the archipelago environments, where the peak of the spectrum is often not well defined (Björkqvist 2020). The wave spectrum was more closely unimodal for the strongest southerly winds, and the peak period therefore matched up well in the case of the highest

significant wave heights (Fig. 10j). The characteristic period has been proposed as an alternative to the instances when the peak period is ill-defined. The validation of the characteristic period showed that it removed a large part of the scatter between the two devices while keeping the bias at a low 0.03 s value (Fig. 10h, Table 5).

Similarly to the peak period, the scatter index was also high for the peak spreading (25%). One major issue in comparing the peak wave direction and spreading of different devices in archipelagos is that, because the spectral peak is ill-defined, one might compare properties of completely different wave components. The validation of the mean direction shows that LP and DWR agree on the wave direction (Fig. 10c). The mean spreading also shows a generally good agreement (Fig. 10g), but with a slight offset corresponding to a bias of 3° (Table 5).

An additional validation of the spectral shape was performed by using the spectral narrowness parameter (κ^2). This parameter was proposed by Battjes and van Vledder (1984) and was found to be suitable for archipelago conditions by Björkqvist et al. (2019). The agreement between DWR and LP was reasonable (Fig. 10i), with a correlation of 0.92 and a bias of -0.02 (Table 5). The scatter index was high (23%), although we are not aware of any other cross-instrumental validation for this particular parameter. Several width parameters are defined using higher moments (Cartwright and Longuet-Higgins 1956) and are therefore sensitive to the high-frequency part of the spectrum. The validation was therefore partially limited by the 0.58 Hz upper frequency of the DWR. In the 0.10–0.58 Hz frequency range, LP spectra tend to be slightly wider than those from the DWR, which might be caused by low-frequency artefacts during low sea states.

The spectral comparison shows a qualitatively good match (Fig. 11) between LP and DWR, except for the low-frequency part where LP has artefacts. During the northerly wind case (Fig. 11a), the peak of the spectrum was roughly at 0.5 Hz, just below the cut-off frequency of the DWR. Above the DWR cut-off frequency, LP spectra followed a f^{-4} tail. For the easterly and

westerly wind events, a clear peak was not defined (Figs. 11b,c), which is a typical situation for the archipelago-type spectrum with many different fetches for a fixed wind direction (Björkqvist 2020). The highest waves measured during the campaign were due to southerly winds, and both the LP and the DWR spectra showed a good match even for the longer waves of a 9 s period (Fig. 11d).

In summary, the validation confirms the accuracy of LP in complex wave conditions. The scatter of the peak parameters is explained more by the ill-defined nature of the parameter than any actual differences between the devices. Otherwise, the validation statistics are similar to those determined for other small buoys when validated against established technologies (Raghukumar et al. 2019; Lancaster et al. 2021).

b. Intercomparison of four moored devices

For an intercomparison of several buoys in the same wave conditions, we moored four buoys in a square layout with a maximum distance of 140 m from each other in places where the water depth was 18–19 m (deduced from nautical charts) (Fig. 6). The buoys were deployed in December and retrieved ten days later in January with a motorboat. The location was chosen due to its openness to long-waves from the Northern Baltic Proper and its gently sloping bottom, which keeps the spatial wave height gradient small.

The mooring consisted of a 60 m rope from the anchor to the surface float and a 20 m rope from the float to the wave buoy. Unfortunately, LP3 started leaking during the field campaign, causing the MEMS sensor not to register data. We exclude this instrument from further analysis. After retrieval, the instrument was cleaned and dried, and subsequent tests showed that no permanent harm was done to the electronics.

The mean wind speed during the measurement campaign was 4.1 ms^{-1}, but gusts at the Pakri weather station reached 16.5 ms^{-1}. During moderate wind speeds (over 6 ms^{-1}), the wind was mainly blowing from north or south. The maximum significant wave height was 1.22 m, and the maximum wave period was 5.97 s (Fig. 12). With the exception of the northerly winds, the waves and wind were misaligned. The misalignment was caused by the slanting fetch (Donelan et al. 1985; Pettersson et al. 2010) and local topography. The slanting fetch also increased the directional spreading, since longer waves usually came from the west even though the short waves were aligned with the wind. For northerly winds, the wave and wind directions aligned, leading to a lower spreading compared to other wind directions.

The wave parameters between the different buoys agreed well (Fig. 12). The R^2 values (between LP1–LP2, LP1–LP4 and LP2–LP4) for significant wave height are over 0.99 and over 0.98 for mean wave period and for directional spreading. The scatter index between H_{m_0} was 3–5 %, reflecting the variability caused by sampling a random process (Donelan and Pierson 1983; Forristall et al. 1996).

The outlier was the mean wave direction of LP1. During the Suomenlinna UAV deployment (described in the next section) the release system malfunctioned and the buoy fell to rocky ground from approximately 2 m. Although bulk omnidirectional parameters and directional spread (which does not depend on true north reference) were reasonable, the yaw angle probably lost its north referencing capabilities, thus rendering the directional estimates unreliable.

c. Deployment with an Unmanned Aerial Vehicle as a drifter

Vääna-Jõesuu (VJ) was the first ever deployment of LP with an UAV (Fig. 13a). The buoy took about 2 hours to drift back to the shore. Significant wave height was about 1 m, which also matched the value from a Copernicus CMEMS product (not shown here).

During the Suomenlinna deployment the buoy was dropped near the moored DWR (Fig. 13b). Wind gusts reached 15 ms^{-1} and the significant wave height was around 1 m with a wave direction from SSW. The buoy drifted until the next day and was picked up from a rocky island with a pilot boat.

At Leppneeme (Fig. 13c), the buoy was deployed from the shore. Although the wave direction was towards the shore, alongshore currents transported the buoy eastward for about 12 hours before it got stuck in pancake ice close to the coast (Fig. 1c). The significant wave height was roughly 0.5 m.

The UAV ground stations were about 2 km from the deployment sites. During these three experiments, we operationally estimated the drift of the buoys with Seatrack Web (https://stw.smhi.se/) and found that the wind leeway coefficient is around 2.5 %, which is in the same range as similar spherical drifting buoys (Sutherland et al. 2020).

In the Gulf of Riga, we deployed three buoys from ice onto ice (Fig. 13d). UAV ground stations were approximately 2 km from shore at locations where pack ice was still safe to walk on. The buoys drifted with ice (with occasionally entering open water) up to month. One buoy stopped sending data 10 days after the deployment because it was brought directly from another (moored) experiment and the battery level was already low. Luckily, locals found it on shore and notified us using the contact information on the buoy. The results from the measurements in ice are described in Section 5d.

The description of the UAV deployment procedures are presented in Appendix C.

d. Waves in ice measurements

We deployed three drifting buoys in the eastern part of the Gulf of Riga (see Section 5c). On 6 March 2021 a strong southwesterly wind event occurred, with the average measured wind speed

and wind gusts being 15 ms^{-1} and 21 ms^{-1}, respectively (Fig. 15a). Sentinel-1 overflights in the morning (04 UTC) and in the evening (16 UTC) showed that the ice edge retreated more than 10 km in about 12 hours (Fig. 14a,b). The Copernicus CMEMS wave field forecast predicted a 2 m significant wave height near the ice edge close to the wave buoys (Fig. 14c). The predicted peak period was 7 s, and the wave direction was between SW and W.

All three buoys started picking up the wave signal at around noon, and in the evening the significant wave height reached up to 1.2 cm at the buoy that was closest to the ice edge (Fig. 15b). The measured energy was above the sensor noise threshold for frequencies 0.10–0.14 Hz, and the surface displacement time series showed identifiable wave groups during the time of the maximum significant wave height (Fig. 15c–d). The roll and pitch angles deviated less than 1°, indicating that the buoys were firmly lodged in ice during the wave event.

6. Discussion

Research and development of prototype miniature wave buoys and loggers has increased in the last decade, e.g., (Loehr et al. 2013; Kennedy et al. 2014; Hirakawa et al. 2016; Centurioni et al. 2017; Yurovsky and Dulov 2017; Farber et al. 2018; Skinner et al. 2018; Zong et al. 2019; Carandell et al. 2020; Cook et al. 2020). Small and affordable emerging wave buoys, like Spotter (Raghukumar et al. 2019) and LP, open up new possibilities for deploying large numbers of buoys simultaneously. With the Spotter, this has already been implemented on oceanic scales through assimilation of wave data in an operational wave model (Houghton et al. 2021; Smit et al. 2021). The ice resistance allows LP to be deployed in the marginal ice zone in large quantities, thus complementing the existing waves-in-ice loggers (Kohout et al. 2015; Rabault et al. 2016; Montiel et al. 2018). This is of utmost importance since our knowledge on wave-ice interactions is still limited due to the low number of measurements made in ice (Squire 2020), especially measurements of the directional

wave spectrum. Wave heights can be very low in the MIZ, and we have shown that a significant wave height of 1 cm is detectable by LP.

In the seasonally ice-covered water bodies, a cause for concern is the fact that operational devices have to be removed before the arrival of ice to avoid damaging the buoys. Nonetheless, the harshest wind conditions, and therefore wave conditions, can typically distort the wave statistics compiled purely from measurements (Björkqvist et al. 2018). Although LP is not designed to replace operational wave buoys, one possible application would be to complement operational measurements by replacing the operational buoy with LP when it is retrieved, thus capturing the open water time before freezing. LP should survive the ice, but if the buoy is lost, the financial implications are not as severe as a loss of an expensive operational buoy, nor do they threaten the continuity of the operational measurements as a whole.

Routine measurements also seldom capture waves shorter than 0.5-0.6 Hz, but LP extends the measurement range to 1.28 Hz (roughly 1 m wavelength). These shorter waves have been extensively studied with specialized research set-ups, e.g., using wave staffs or polarimetric cameras. The reason for the persistent scientific interest for this part of the wave regime is its decisive impact on many sea-atmosphere processes. Waves between 0.58 – 1.28 Hz have been shown to contribute 26 % of the so-called Stokes drift (Lenain and Pizzo 2020), and they also carry a significant part of the wave-induced stress (Janssen 1991; Mueller and Veron 2009). These processes then affect the drift of the object, oil and other surfactants and enhance the upper-layer turbulence and mixing, thus contributing to the sea-atmosphere fluxes of e.g., CO_2. One possible niche for LP could be regions like archipelagos, fjords or small lakes. In these areas, the short waves can carry a major part of the total wave energy, but establishing elaborate research wave measurement stations might not be feasible. From a practical perspective, the measurement of the high-frequency part might

require cleaning of the buoy after some time to avoid accumulation of added mass and change of the buoy dimensions due to bio-fouling (Thomson et al. 2015; Campos et al. 2021).

Peak wave periods can reach 25 s in the world oceans (Hanafin et al. 2012), but low-frequency noise in wave measurements are unfortunately a common feature. Ashton and Johanning (2015) found spurious low-frequency energy caused by high drift forces brought about by currents and mooring. Low-frequency artefacts can also be created by a loss of the GPS-signal in buoys that use the Doppler shift to measure the buoy velocity, e.g., the DWR-G4 (Björkqvist et al. 2016). We found that the MEMS sensor of the LP also suffers from low-frequency noise. This noise comes from the gyroscope random noise, which affects the pitch, roll and yaw angles. These angles are then used to calculate the free acceleration inside the sensor, and the noise is further amplified by double integration. Low-frequency noise was also present in drifting buoys.

Yurovsky and Dulov (2020) also identified low-frequency noise, but didn't present any correction method. Earle and Bush (1982) and Lang (1987) proposed a method for denoising by subtracting energy present at low-frequencies from higher frequency. By comparing several months of LP measurements to coinciding Waverider measurements, we concluded that a large part of the low-frequency noise in the spectrum is actually variance density that is somehow redistributed from higher frequencies. When the low frequency part was denoised, we quantified the amount of variance that was lost and re-introduced this variance back to the higher frequencies in proportion to the already existing variance (see Appendix B). This correction was performed in Fourier space, which means that already the time series, determined through the inverse transform after integration in Fourier space was corrected. Although this method is partially ad hoc, it was shown to correct the final spectrum for both dominant waves and the spectral tail. Nonetheless, further development, not excluding changing the MEMS sensor, is currently pursued.

Non-typical deployments, such as aerial deployments by UAVs, have recently been used as an additional tool in observational studies (Zappa et al. 2020). UAVs are gaining popularity since they can carry lightweight sensors (Fuertes et al. 2019). These innovative solutions are partially motivated by environmental concerns, but they also allow to bypass the cost of a ship. Because of its low weight, LP can be deployed by an industrial UAV as a drifter. It has already been tested in deployments from shore and from sea ice with the deployment range extending to 2 km. These novel deployment techniques are still being established, but possible applications can include collecting data from surf zones or transporting a buoy onto the MIZ. UAV deployments will continue to be one part of the further development of LP.

It is possible to extend the operation time of LP by replacing rechargeable Li-ion batteries with Lithium-Thionyl chloride primary batteries. These batteries have an energy density that is about 2.5 times higher than that of rechargeable ones. This would extend the autonomous operating time to 5 months and make measurements in remote locations more feasible. Also, the buoy leaked on two occasions over the course of 18 field deployments. These incidents have been accounted for when designing the new hull (Fig. 16). The new hull is made of molded plastic and has a sealing O-ring on the top. External connectors for charging and accessing data have been added to remove the need for opening the buoy and to enhance usability. The inertial sensor, electronics and measurement methodology are kept the same. First laboratory tests of the new design on durability and waterproofness have been carried out successfully, but further testing is ongoing to validate this new design in the field.

7. Conclusions

A wave buoy (LainePoiss, LP) was developed. LP weighs 3.5 kg, measures waves up to 1.28 Hz, has a rechargeable battery with 2 months of operation, and transmits wave parameters and spectra operationally over cellular or satellite networks. From our study, we can conclude the following:

- Wave parameters measured in the field were in good accordance with those measured by a nearby Directional Waverider: the bias of H_{m_0} was 0.01 m, correlation 0.99 and scatter index of 8%. $T_{m_{-10}}$ bias 0.14 s, correlation 0.98 and scatter index 4 %. The mean absolute deviation of mean wave direction was 7°.

- The high frequency part of the spectrum (up to 1.28 Hz) compared well to a wave gauge in the wave tank. The wave spectrum of LP was validated up to a Waverider cut-off frequency of 0.58 Hz in the field, and the spectral tail of LP had an expected power-law behavior up to 1.28 Hz.

- LP can measure waves in ice with a significant wave height as low as 1 cm. This was confirmed in an over a month-long experiment where several LP's were deployed in ice in the Baltic Sea.

- Because of its low weight, LP can be deployed as a drifter to a distance of at least 2 km using an Unmanned Aerial Vehicle (UAV).

Noise in the gyroscopic sensor resulted in low-frequency artefacts, but the displacement time series can be corrected (see Appendix B). We will continue testing the wave buoy and expand our measurement areas outside of the Baltic Sea to capture longer waves. Depending on the MEMS sensor noise levels in these conditions, we can decide whether to replace the wave buoy's sensor for one with several times less noise.

Acknowledgments. This work was supported by the Personal Research Funding of the Estonian Ministry of Education and Research (grant number PSG22).

We would like to thank Lauri Laakso and Roine Tuomo for helping with Suomenlinna field experiments. We appreciate discussions with Kimmo Kahma. We thank Rivo Uiboupin, Jüri Elken, Aarne Männik and Sigrid Aas for keeping the administrative matters under control. We thank Tarmo Kõuts for helping us with the first versions of real-time display of data on a website. The first author thanks (little) Aran Alari for inspiring the wave buoy name LP.

We thank the following institutions and enterprises for their successful participation in the applications of LainePoiss: the Maritime Administration of Estonia, the Estonian Environment Agency, AS Saarte Liinid, OÜ Lainemudel, TalTech Small Craft Competence Centre and the City of Helsinki.

Valdur Kaldvee and Kristjan Mölder are the founders, and the sole owners and employees of WiseParker OÜ who produce the LainePoiss wave buoy presented in this manuscript. The development of LainePoiss has been made in co-operation with Tallinn University of Technology

Data availability statement. The data used in this manuscript will be made openly available upon the publication of the final paper.

APPENDIX A

Statistical parameters

With N is the number of data points we used the following statistical parameters:

$$\text{Mean} = \overline{x_i} = \frac{1}{N}\sum_i x_i, \tag{A1}$$

For angular quantities, θ, the mean is defined as

$$\overline{\theta_i} = \arctan\left(\frac{\overline{\sin(\theta_i)}}{\overline{\cos(\theta_i)}}\right). \tag{A2}$$

and the difference

$$|\theta_1 - \theta_2| = \min\{|\theta_1 - \theta_2|, 360 - |\theta_1 - \theta_2|\}. \tag{A3}$$

The covariance is

$$\mathrm{Cov}(x_i, r_i) = \sqrt{\frac{1}{N-1}\sum_i (x_i - \overline{x_i})(r_i - \overline{r_i})}. \tag{A4}$$

where x_i are observations and r_i are the reference values (typically from the Waverider).

The variance and standard deviation are

$$\mathrm{Var}(x_i) = \mathrm{Cov}(x_i, x_i), \tag{A5}$$

$$\mathrm{Std}(x_i) = \sqrt{\mathrm{Var}(x_i)}, \tag{A6}$$

For cross-comparison of data sets, we defined the following parameters:

$$\mathrm{Bias} = \overline{x_i} - \overline{r_i}, \tag{A7}$$

The root-mean-square deviation, mean absolute deviation and scatter index (in percent) are defined:

$$\mathrm{RMSD} = \sqrt{\frac{1}{N}\sum_i (x_i - r_i)^2}, \tag{A8}$$

$$\mathrm{MAD} = \frac{\sum_i |x_i - r_i|}{N}, \tag{A9}$$

$$\mathrm{SI} = 100 \sqrt{\frac{\sum_i \left[(x_i - \overline{x_i}) - (r_i - \overline{r_i})\right]^2}{\sum_i r_i^2}}, \tag{A10}$$

The slope is defined as a least-squares-fit $x = Kr$

$$K = \frac{\sum_i x_i r_i}{\sum_i r_i^2}, \tag{A11}$$

and the Pearson correlation coefficient is

$$\mathrm{R} = \frac{\mathrm{Cov}(\mathrm{x_i}, \mathrm{r_i})}{\mathrm{Std}(x_i)\mathrm{Std}(r_i)}. \tag{A12}$$

APPENDIX B

Renormalization in integration

The limitations of the sensor create low-frequency noise, but we have concluded that this noise is actually a misplaced signal from other frequencies. If the low-frequency noise is removed, it should be added back to the frequencies, so that the power spectrum fulfills the following:

$$E(f) = E_0(f) + \frac{\Delta\varepsilon E_0(f)}{\sum_f E_0(f)} \tag{B1}$$

$$= E_0(f)\left(1 + \frac{\Delta\varepsilon}{\sum_f E_0(f)}\right), \tag{B2}$$

where

$$\Delta\varepsilon = \sum_f \hat{E}(f) - \sum_f E_0(f), \tag{B3}$$

and $\hat{E}(f)$ and $E_0(f)$ are the power spectra of the unprocessed and denoised signals. $\Delta\varepsilon$ quantifies how much variance density of the signal has been lost. Especially, if $\Delta\varepsilon = 0$ then no further correction is necessary.

In practise, this denoising and compensation is performed during the integration, which results in a clean displacement signal from which the power spectrum can be calculated in a normal fashion without having to deal with the above compensation after the fact.

Low frequency acceleration data is first denoised using the following procedure: the average squared Fourier amplitude is calculated for the frequencies 1/100 to 1/30 Hz.

$$\alpha = \langle |\hat{A}(f)|^2 \rangle_{1/100 \leq f \leq 1/30} \tag{B4}$$

where $\hat{A}(f) = \mathcal{F}[a(t)]$ is the Fourier transform of the acceleration signal and $|\hat{A}(f)|$ is its modulus.

This mean value (the noise) is then removed from the Fourier transform by

$$A_0(f) = \max\{0, \hat{A}(f) \frac{\hat{A}(f) - \alpha \cdot \left(1 - R_f(f)\right)}{\hat{A}(f)}\}, \tag{B5}$$

where $R(f)$ is a response function:

$$R_f(f) = \begin{cases} 0, & 0 < f < f_1 \\ \frac{1}{2}\left[1 - \cos\left(\pi \frac{f - f_1}{f_2 - f_1}\right)\right] & f_1 \leq f \leq f_2 \\ 1 & f_2 < f \leq f_N \end{cases} \tag{B6}$$

Here $f_1 = 0.08$ Hz and $f_1 = 0.10$ Hz. In other words, the Fourier transform for $f > 0.10$ Hz is not touched.

Following e.g. Rabault et al. (2020), the acceleration values are then integrated in Fourier space:

$$X_0(f) = -A_0(f) R_f(f) \cdot (2\pi f)^{-2} \tag{B7}$$

$$\hat{X}(f) = -\hat{A}(f) R_f(f) \cdot (2\pi f)^{-2}, \tag{B8}$$

where $f_1 = 0.05$ Hz and $f_2 = 0.06$ Hz in the response function $R_f(f)$.

That is, $\hat{X}(f)$ and $X_0(f)$ are now the uncorrected and denoised Fourier transform of the displacement signal. We quantify how much of the squared amplitudes of the signal were lost by the low-frequency correction:

$$\Delta\mathcal{X}^2 = \sum_f |\hat{X}(f)|^2 - \sum_f |X_0(f)|^2. \tag{B9}$$

This lost signal information will be added back in a way that will compensate the power spectrum as outlined in Eq. B2:

$$\begin{aligned} X(f) &= X_0(f)\sqrt{1 + \frac{\Delta\mathcal{X}^2}{\sum_f |X_0(f)|^2}} && \text{(B10)} \\ &= X_0(f)\sqrt{1 + \frac{\sum_f |\hat{X}(f)|^2 - \sum_f |X_0(f)|^2}{\sum_f |X_0(f)|^2}} && \text{(B11)} \\ &= X_0(f)\sqrt{1 + \frac{\sum_f |\hat{X}(f)|^2}{\sum_f |X_0(f)|^2} - 1} && \text{(B12)} \\ &= X_0(f)\sqrt{\frac{\sum_f |\hat{X}(f)|^2}{\sum_f |X_0(f)|^2}}. && \text{(B13)} \end{aligned}$$

The displacement time series is then given by the inverse Fourier transform:

$$x(t) = \mathcal{F}^{-1}[X(f)]. \tag{B14}$$

This time series is now corrected for the low-frequency artefacts, which has been redistributed to the other frequencies. The power spectrum or any other statistics can now be calculated from this displacement time series without further corrections.

APPENDIX C

Experiences from UAV deployments

In this appendix, we document our experiences from six events where an industrial Unmanned Aerial Vehicle (UAV) was used to deploy LainePoiss (LP) as a floating device. Our deployments were made in Estonia and Finland during 2019–2021. The guidelines and regulations governing the use of UAV's change and differ from country to country, especially outside of the European Union. Make sure to get correct information and follow any local laws and ordinances when considering deploying LP with an UAV. Also note that the steps below do not guarantee a safe or successful deployment.

The UAV should be regularly maintained to be sure of the condition of the equipment; motors, blades, batteries and the remote controller have to be working properly. Firmware and software should also be up to date. Notifications through e.g., the remote controller or pilot application should be taken seriously, and they need to be resolved before flight. Before deploying the actual device, we recommend practising with, e.g., sand bags that have the same weight as LP.

A successful UAV deployment starts with a comprehensive preparation and plan for the flight and requires at least two persons. The first person flies the drone while the second person assists at lift-off and landing. We used a DJI Matrice 600 Pro industrial drone with a release mechanism (Fig. 1b). A 5 m long fishing thread (we used Dyneema 0.3 mm with a breaking strength of 25 kg) was found suitable for connecting the UAV and the wave buoy. A longer thread could make releasing the LP more convenient as the UAV can be higher, thus having a stronger signal strength. Nonetheless, a shorter thread minimizes the motion of the buoy during flight. The lift-off is the riskiest part: the second person has to hold the thread downwind and low to the ground to minimize the risk of the thread being caught by the UAV motors. This has to be done while keeping a distance of at least a few meters from the UAV. For the safety of the assisting person, the pilot should guide

the UAV upwards for the first couple of meters as quickly as possible. The rest of the lift-off can happen at a slower pace until the wave buoy is up in the air. We used a flight height of 20–30 m when transporting the wave buoy to the drop-off location.

With fully charged batteries at lift-off, we deployed the buoy at a distance of up to 2 km. We started guiding the UAV back towards the ground station before the battery dropped below 50 %. In our deployments we flew upwind with the heavy weight, thus returning to the ground station downwind. We found that the battery charge at landing was still at about 20 %.

Below is a step-by-step checklist that we have used in our deployments:

- The pilot does an UAV pre-check a day before flight as well as on the field. If applicable, follow the messages from the pilot application.
- The second person, crouching at least 2 m from the UAV, holds the thread under tension between the UAV and the person's hand, ready to give slack as the UAV is ascending.
- The pilot loudly notifies the other persons before activating motors and makes sure everybody is ready for lift-off.
- The pilot ascends the first two meters as quickly as possible, and the second person gives slack to the thread as the UAV takes off.
- A second person must hold the thread under tension between the UAV and their hand until the LP is up in the air.
- Thread should be downwind, even though the UAV might deviate also downwind where the second person is holding the thread.

Recommendations for the pilot:

- Flight height between 20–30 meters.

- Do not fly further than 50% of the battery capacity; ideally fly upwind with payload and return with tailwind.

References

Ashton, I., and L. Johanning, 2015: On errors in low frequency wave measurements from wave buoys. *Ocean Engineering*, **95**, 11–22, doi:https://doi.org/10.1016/j.oceaneng.2014.11.033.

Battjes, J. A., and G. P. van Vledder, 1984: Verification of Kimura's Theory for Wave Group Statistics. *Proc. 19th Int. Conf. Coastal Engineering*, ASCE, New York, 642–648, doi:10.1061/9780872624382.044.

Bishop, C. T., and M. A. Donelan, 1987: Measuring waves with pressure transducers. *Coastal Engineering*, **11 (4)**, 309–328.

Björkqvist, J.-V., 2020: Waves in Archipelagos. Ph.D. thesis, FMI Contributions 159, University of Helsinki.

Björkqvist, J.-V., I. Lukas, V. Alari, G. P. van Vledder, S. Hulst, H. Pettersson, A. Behrens, and A. Männik, 2018: Comparing a 41-year model hindcast with decades of wave measurements from the baltic sea. *Ocean Engineering*, **152**, 57–71.

Björkqvist, J.-V., H. Pettersson, and K. K. Kahma, 2019: The wave spectrum in archipelagos. *Ocean Science*, **15 (6)**, 1469–1487.

Björkqvist, J.-V., H. Pettersson, L. Laakso, K. K. Kahma, H. Jokinen, and P. Kosloff, 2016: Removing low-frequency artefacts from datawell dwr-g4 wave buoy measurements. *Geosci. Instrum., Methods Data Syst.*, **5 (1)**, 17–25, doi:10.5194/gi-5-17-2016.

Campos, R. M., H. Islam, T. R. Ferreira, and C. Guedes Soares, 2021: Impact of heavy biofouling on a nearshore heave-pitch-roll wave buoy performance. *Applied Ocean Research*, **107**, 102 500, doi:https://doi.org/10.1016/j.apor.2020.102500.

Carandell, M., D. M. Toma, J. P. Pinto, M. Gasulla, and J. del Río, 2020: Impact on the wave parameters estimation of a kinetic energy harvester embedded into a drifter. *Global Oceans 2020: Singapore–US Gulf Coast*, IEEE, 1–6.

Cartwright, D. E., and M. S. Longuet-Higgins, 1956: The statistical distribution of the maxima of a random function. *Proceedings of the royal society of london. series a. mathematical and physical sciences*, **237 (1209)**, 212–232, doi:https://doi.org/10.1098/rspa.1956.0173.

Cavaleri, L., 1980: Wave measurement using pressure transducer. *Oceanologica Acta*, **3 (3)**, 339–346.

Centurioni, L., L. Braasch, E. Di Lauro, P. Contestabile, F. De Leo, R. Casotti, L. Franco, and D. Vicinanza, 2017: A new strategic wave measurement station off naples port main breakwater. *Coast. Eng. Proc. 1*, **36**.

Christakos, K., J.-V. Björkqvist, L. Tuomi, B. R. Furevik, and Ø. Breivik, 2021: Modelling wave growth in narrow fetch geometries: The white-capping and wind input formulations. *Ocean Modelling*, **157**, 101 730.

Cook, A., A. Babanin, D. Sgarioto, P. Graham, J. Mathew, A. Skvortsov, R. Manasseh, and D. Tothova, 2020: A uav 'mobile buoy'for measuring surface waves. *22nd Australasian Fluid Mechanics Conference AFMC2020*, The University of Queensland, doi:https://doi.org/10.14264/8e7141e.

Donelan, M. A., J. Hamilton, and W. H. Hui, 1985: Directional Spectra of Wind-Generated Waves. *Philosophical Transactions of the Royal Society A: Mathematical, Physical and Engineering Sciences*, **315 (1534)**, 509–562, doi:10.1098/rsta.1985.0054.

Donelan, M. A., and W. J. Pierson, 1983: The Sampling Variability of Estimates of Spectra of Wind-Generated Gravity Waves. *Journal of Geophysical Research*, **88 (C7)**, 4381–4392, doi:10.1029/JC088iC07p04381.

Earle, M., and K. Bush, 1982: Strapped-down accelerometer effects on ndbo wave measurements. *OCEANS 82*, 838–848, doi:10.1109/OCEANS.1982.1151908.

Farber, S., H. Allaka, I. Klein, and M. Groper, 2018: Estimating sea state using a low cost buoy. *2018 IEEE International Conference on the Science of Electrical Engineering in Israel (ICSEE)*, IEEE, 1–5.

Forristall, G. Z., J. C. Heideman, I. M. Leggett, B. Roskam, and L. Vanderschuren, 1996: Effect of sampling variability on hindcast and measured wave heights. *Journal of waterway, port, coastal, and ocean engineering*, **122 (5)**, 216–225.

Fuertes, F. C., L. Wilhelm, and F. Porté-Agel, 2019: Multirotor uav-based platform for the measurement of atmospheric turbulence: Validation and signature detection of tip vortices of wind turbine blades. *Journal of Atmospheric and Oceanic Technology*, **36 (6)**, 941–955.

Gordon, L., and A. Lohrmann, 2002: Near-shore doppler current meter wave spectra. *Proceedings of the International Symposium on Ocean Wave Measurement and Analysis*, **1**, doi:10.1061/40604(273)4.

Graber, H. C., E. A. Terray, M. A. Donelan, W. M. Drennan, J. C. Van Leer, D. B. Peters, and J. C. V. Leer, 2000: ASIS—A New Air–Sea Interaction Spar Buoy: Design and Per-

formance at Sea. *Journal of Atmospheric and Oceanic Technology*, **17 (5)**, 708–720, doi: 10.1175/1520-0426(2000)017<0708:AANASI>2.0.CO;2.

Hanafin, J. A., and Coauthors, 2012: Phenomenal sea states and swell from a north atlantic storm in february 2011: A comprehensive analysis. *Bulletin of the American Meteorological Society*, **93 (12)**, 1825 – 1832, doi:10.1175/BAMS-D-11-00128.1.

Herbers, T. H. C., P. F. Jessen, T. T. Janssen, D. B. Colbert, and J. H. MacMahan, 2012: Observing Ocean Surface Waves with GPS-Tracked Buoys. *J. Atmos. Oceanic Technol.*, **29 (7)**, 944–959, doi:10.1175/JTECH-D-11-00128.1.

Hirakawa, Y., T. Takayama, T. Hirayama, and H. Susaki, 2016: Development of mini-buoy for short term measurement of ocean wave. *OCEANS 2016 MTS/IEEE Monterey*, IEEE, 1–4.

Holthuijsen, L., 2007: *Waves in Oceanic and Coastal Waters*. Cambridge University Press, Cambridge, 387 pp.

Houghton, I., P. Smit, D. Clark, C. Dunning, A. Fisher, N. Nidzieko, P. Chamberlain, and T. Janssen, 2021: Performance statistics of a real-time pacific ocean weather sensor network. *Journal of Atmospheric and Oceanic Technology*, **38 (5)**, 1047–1058.

Janssen, P. A., 1991: Quasi-linear Theory of Wind-Wave Generation Applied to Wave Forecasting. *Journal of Physical Oceanography*, **21 (11)**, 1631–1642, doi:10.1175/1520-0485(1991)021<1631:QLTOWW>2.0.CO;2.

Kennedy, D., M. Walsh, and B. O'Flynn, 2014: Development of a miniature, low-cost wave measurement solution. *2014 Oceans-St. John's*, IEEE, 1–6.

Kodaira, T., T. Waseda, T. Nose, K. Sato, J. Inoue, J. Voermans, and A. Babanin, 2020: Observation of on-ice wind waves under grease ice in the western arctic ocean. *Polar Science*, 100567.

690 Kohout, A. L., B. Penrose, S. Penrose, and M. J. Williams, 2015: A device for measuring wave-
691 induced motion of ice floes in the antarctic marginal ice zone. *Annals of Glaciology*, **56 (69)**,
692 415–424.

693 Lancaster, O., R. Cossu, S. Boulay, S. Hunter, and T. E. Baldock, 2021: Comparative wave
694 measurements at a wave energy site with a recently developed low-cost wave buoy (spotter),
695 adcp, and pressure loggers. *Journal of Atmospheric and Oceanic Technology*, **38 (5)**, 1019–
696 1033.

697 Lang, N., 1987: The empirical determination of a noise function for ndbc buoys with strapped-down
698 accelerometers. *OCEANS'87*, IEEE, 225–228.

699 Lenain, L., and N. Pizzo, 2020: The contribution of high-frequency wind-generated surface
700 waves to the stokes drift. *Journal of Physical Oceanography*, **50 (12)**, 3455 – 3465, doi:
701 10.1175/JPO-D-20-0116.1.

702 Loehr, H., S. Boulay, W. Warner, D. Johnson, B. Beamlsey, P. Mccomb, and Coauthors, 2013:
703 Development of a low cost wave buoy by utilising smartphone technology. *Coasts and Ports*
704 *2013: 21st Australasian Coastal and Ocean Engineering Conference and the 14th Australasian*
705 *Port and Harbour Conference*, Engineers Australia, 116.

706 Longuet-Higgins, M. S., 1961: Observations of the directional spectrum of sea waves using the
707 motions of a floating buoy. *Ocean wave spectra*.

708 Montiel, F., V. Squire, M. Doble, J. Thomson, and P. Wadhams, 2018: Attenuation and directional
709 spreading of ocean waves during a storm event in the autumn beaufort sea marginal ice zone.
710 *Journal of Geophysical Research: Oceans*, **123 (8)**, 5912–5932.

Mueller, J. A., and F. Veron, 2009: Nonlinear formulation of the bulk surface stress over breaking waves: Feedback mechanisms from air-flow separation. *Boundary-Layer Meteorology*, **130 (1)**, 117–134, doi:10.1007/s10546-008-9334-6.

Munk, W. H., 1950: Origin and generation of waves. *Proc. 1 st Conf. Coastal Engineering*, Long Beach, ASCE, Vol. 1, 1-4, doi:10.9753/icce.v1.1.

Pearman, D., T. Herbers, T. Janssen, H. van Ettinger, S. McIntyre, and P. Jessen, 2014: Drifter observations of the effects of shoals and tidal-currents on wave evolution in san francisco bight. *Continental Shelf Research*, **91**, 109–119.

Pettersson, H., K. K. Kahma, and L. Tuomi, 2010: Wave directions in a narrow bay. *Journal of Physical Oceanography*, **40 (1)**, 155–169.

Rabault, J., G. Sutherland, O. Gundersen, A. Jensen, A. Marchenko, and Øyvind Breivik, 2020: An open source, versatile, affordable waves in ice instrument for scientific measurements in the polar regions. *Cold Regions Science and Technology*, **170**, 102 955, doi:https://doi.org/10.1016/j.coldregions.2019.102955.

Rabault, J., G. Sutherland, B. Ward, K. H. Christensen, T. Halsne, and A. Jensen, 2016: Measurements of waves in landfast ice using inertial motion units. *IEEE Transactions on Geoscience and Remote Sensing*, **54 (11)**, 6399–6408.

Raghukumar, K., G. Chang, F. Spada, C. Jones, T. Janssen, and A. Gans, 2019: Performance characteristics of "spotter," a newly developed real-time wave measurement buoy. *J. Atmos. Oceanic Technol.*, **36 (6)**, 1127–1141, doi:10.1175/JTECH-D-18-0151.1.

Skinner, E., M. Rooney, and M. Hinders, 2018: Low-cost wave characterization modules for oil spill response. *Journal of Ocean Engineering and Science*, **3 (2)**, 96–108.

Smit, P., I. Houghton, K. Jordanova, T. Portwood, E. Shapiro, D. Clark, M. Sosa, and T. Janssen, 2021: Assimilation of significant wave height from distributed ocean wave sensors. *Ocean Modelling*, **159**, 101 738.

Squire, V. A., 2020: Ocean wave interactions with sea ice: a reappraisal. *Annual Review of Fluid Mechanics*, **52**, 37–60.

Sutherland, G., and Coauthors, 2020: Evaluating the leeway coefficient of ocean drifters using operational marine environmental prediction systems. *Journal of Atmospheric and Oceanic Technology*, **37 (11)**, 1943–1954.

Thomson, J., 2012: Wave breaking dissipation observed with "swift" drifters. *Journal of Atmospheric and Oceanic Technology*, **29 (12)**, 1866–1882.

Thomson, J., and Coauthors, 2015: Biofouling effects on the response of a wave measurement buoy in deep water. *Journal of Atmospheric and Oceanic Technology*, **32 (6)**, 1281–1286.

Veras Guimarães, P., and Coauthors, 2018: A surface kinematics buoy (skib) for wave–current interaction studies. *Ocean Science*, **14 (6)**, 1449–1460.

Voermans, J., P. Smit, T. Janssen, and A. Babanin, 2020: Estimating wind speed and direction using wave spectra. *Journal of Geophysical Research: Oceans*, **125 (2)**, e2019JC015 717.

Wadhams, P., 1978: Wave decay in the marginal ice zone measured from a submarine. *Deep Sea Research*, **25 (1)**, 23–40.

Young, I. R., 1995: The determination of confidence limits associated with estimates of the spectral peak frequency. *Ocean Engineering*, **22 (7)**, 669–686, doi:10.1016/0029-8018(95)00002-3.

753 Yurovsky, Y. Y., and V. Dulov, 2017: Compact low-cost arduino-based buoy for sea surface wave
754 measurements. *2017 Progress in Electromagnetics Research Symposium-Fall (PIERS-FALL)*,
755 IEEE, 2315–2322.

756 Yurovsky, Y. Y., and V. A. Dulov, 2020: Mems-based wave buoy: Towards short wind-wave sensing.
757 *Ocean Engineering*, **217**, 108 043, doi:https://doi.org/10.1016/j.oceaneng.2020.108043.

758 Zappa, C. J., S. M. Brown, N. J. M. Laxague, T. Dhakal, R. A. Harris, A. M. Farber, and
759 A. Subramaniam, 2020: Using ship-deployed high-endurance unmanned aerial vehicles for the
760 study of ocean surface and atmospheric boundary layer processes. *Frontiers in Marine Science*,
761 **6**, 777, doi:10.3389/fmars.2019.00777.

762 Zong, Y., H.-Y. Cheng, H. Chien, and B. Koppe, 2019: Miniature wave buoy–laboratory and
763 field tests for development of a robust low-cost measuring technique. *Coastal Structures 2019*,
764 453–462.

LIST OF TABLES

TABLE 1. Testbench results

Wave period (s)	Prescribed amplitude (mm)	Measured amplitude (mm)
1	68	69
5	68	66
10	68	64
20	68	64
25	68	64

779 TABLE 2. Wave tank results. H_{m_0} was integrated between 0.30-1.28 Hz. The peak frequency (f_p) corresponds
780 to the wave gauge

	Wave gauge	LP1	LP3 (moored)	LP4
	H_{m_0} (m)	H_{m_0} (m)	H_{m_0} (m)	H_{m_0} (m)
f_p = 0.57 Hz	0.15	0.16	0.16	0.16
f_p = 0.63 Hz	0.16	0.15	0.17	0.16
f_p = 0.53 Hz	0.17	0.19	0.20	0.20
f_p = 0.53 Hz	0.17	0.19	0.20	0.19
f_p = 0.77 Hz	0.07	0.07	0.07	0.07
f_p = 0.77 Hz	0.06	0.08	0.07	0.07
f_p = 0.87 Hz	0.09	0.11	0.11	0.10
f_p = 0.73 Hz	0.10	0.10	0.11	0.10

TABLE 3. An overview of the field experiments where LainePoiss was moored.

	Deployment 1	Deployment 2	Deployment 3	Deployment 4
Device	LP1–LP2	LP3	LP4	LP1–LP4
Location	Suomenlinna (S1–S2)	Suomenlinna (S1)	Suomenlinna (S1)	Vääna-Jõesuu (V1–V4)
Depth	17 m	17 m	17 m	19 m
Period	18.6.–24.7.2020	14.8.–21.9.2020	24.9.–24.11.2020	22.12.2020–03.01.2021
Mean U_{10}	6.3 ms^{-1}	7.3 ms^{-1}	8.2 ms^{-1}	4.1 ms^{-1}
Mean H_{m_0}	0.32 m	0.39 m	0.50 m	0.51 m
Mean T_c	4.5 s	4.4 s	4.3 s	5.8 s

781 TABLE 4. LainePoiss and DWR statistics during the deployments (N=6357). N is smaller than the one used
782 in the validation statistics Table 5 because in June-July 2020 two LP's were simultaneously measuring. In the
783 validation, both buoys were included against the comparison with DWR, here only LP #1 is used (eastern buoy,
784 Fig. 6).

	LP / WR	LP / WR	LP / WR	LP / WR
Parameter	Mean	Std	Min	Max
H_{m_0} (m)	0.42 / 0.42	0.27 / 0.29	0.04 / 0.03	1.84 / 1.90
$T_{m_{02}}$ (s)	3.05 / 2.91	0.40 / 0.43	2.11 / 1.91	4.87 / 4.53
$T_{m_{01}}$ (s)	3.26 / 3.06	0.46 / 0.49	2.17 / 1.93	5.48 / 4.84
$T_{m_{-10}}$ (s)	3.84 / 3.44	0.61 / 0.59	2.44 / 2.05	6.73 / 5.86
T_c (s)	4.40 / 3.83	1.49 / 1.12	1.87 / 1.74	9.53 / 8.32
T_p (s)	4.72 / 3.99	2.10 / 1.41	1.72 / 1.72	10.00 / 8.54
κ^2 (-)	0.11 / 0.13	0.09 / 0.10	0.00 / 0.00	0.59 / 0.68
σ_m (°)	45 / 41	12 / 11	27 / 23	80 / 80
σ_p (°)	38 / 32	15 / 9	11 / 9	81 / 80
Parameter	Mode	Std	Min	Max
θ_m (°)	202 / 198	45 / 44	5 / 1	359 / 359
θ_p (°)	202 / 200	52 / 49	0 / 0	359 / 358

TABLE 5. Validation statistics. N=7486 for H_{m_0}. For other parameters, only cases where the DWR measured H_{m_0} >0.25 m were included (N=4827).

Parameter	Bias	RMSD	SI (%)	Slope	R
H_{m_0} (m)	0.01	0.04	8	0.99	0.99
$T_{m_{02}}$ (s)	0.06	0.10	3	1.02	0.98
$T_{m_{01}}$ (s)	0.08	0.12	3	1.02	0.98
$T_{m_{-10}}$ (s)	0.16	0.23	5	1.04	0.96
T_c (s)	0.03	0.35	9	1.01	0.91
T_p (s)	0.03	0.89	21	0.99	0.66
κ^2 (-)	-0.02	0.04	23	0.85	0.92
σ_m (°)	3	5	9	1.09	0.88
σ_p (°)	2	8	25	1.03	0.49
Parameter	|Bias|	MAD			
θ_m (°)	1	7			
θ_p (°)	2	11			

787 TABLE 6. An overview of drifting experiments where LainePoiss was deployed using an UAV. GoR refers to
788 the Gulf of Riga.

	Deployment 1	Deployment 2	Deployment 3	Deployment 4	Deployment 5	Deployment 6
Device	LP1	LP1	LP5	LP2	LP5	LP6
Location	Vääna-Jõesuu (VJ)	Suomenlinna (SO)	Leppneeme	GoR	GoR	GoR
Type	Drifting	Drifting	Drifting	Drifting	Drifting	Drifting
Period	15.08.2019	06.12–07.12 2019	27.02-28.02 2021	03.03-11.03 2021	03.03-05.04	03.03-30.03
Mean U_{10}	8 ms^{-1}	13 ms^{-1}	8 ms^{-1}	In ice	In ice	In ice
Mean H_{m_0}	0.94 m	0.87 m	0.41 m	In ice	In ice	In ice
Mean $T_{m_{-10}}$	4.2 s	4.4 s	2.7 s	In ice	In ice	In ice

LIST OF FIGURES

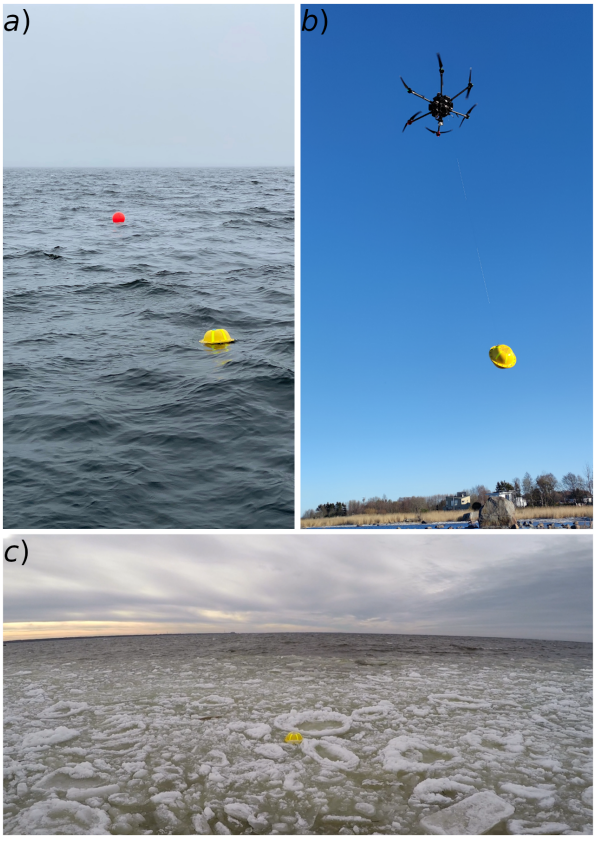

FIG. 1. a) LainePoiss in a moored configuration; b) transporting with an UAV and c) drifted to pancake ice.

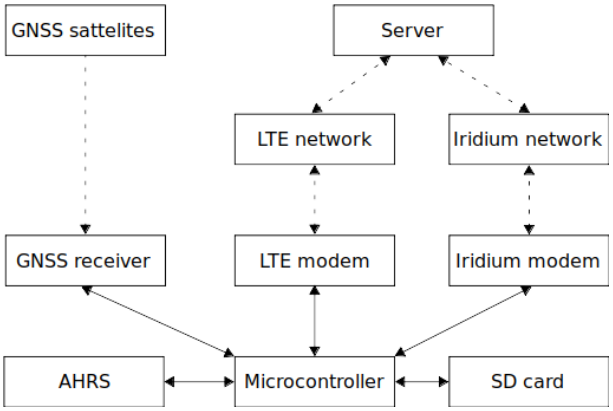

FIG. 2. Scheme of the electronics components of the buoy.

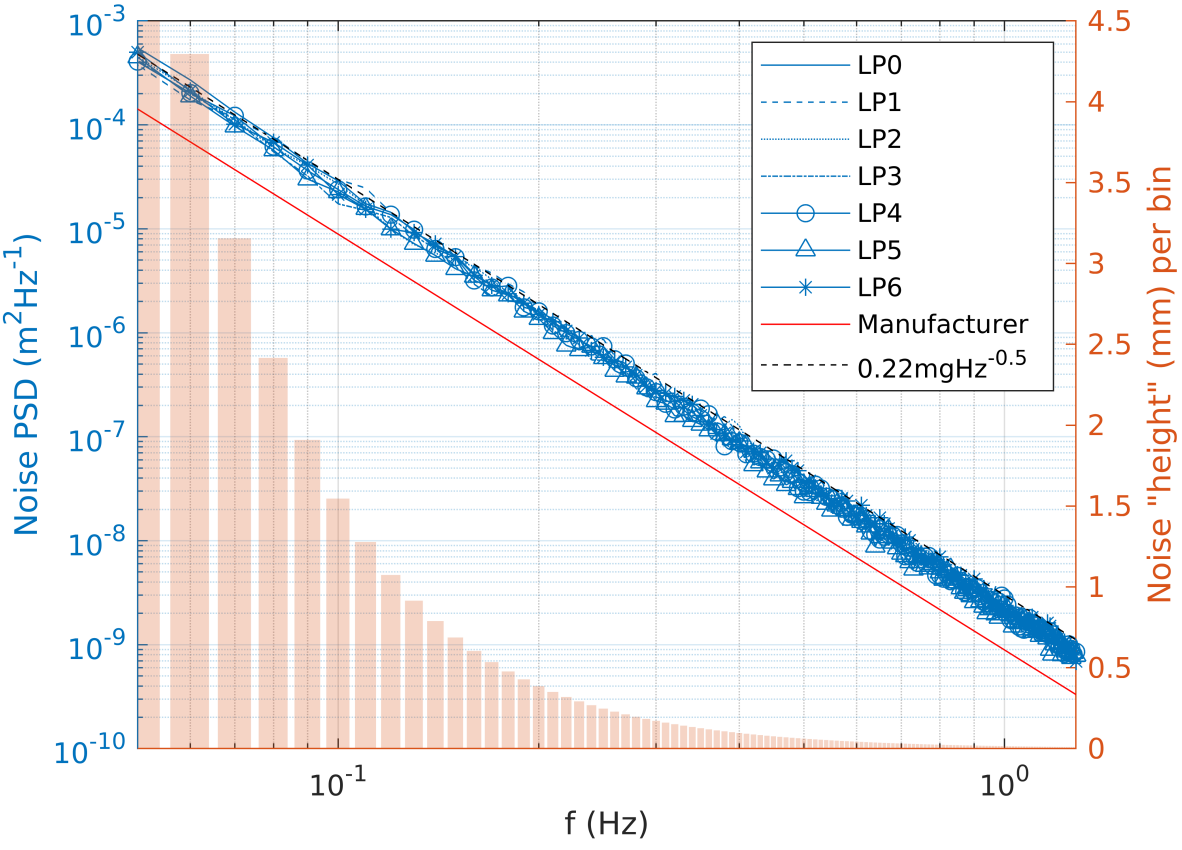

828 FIG. 3. Noise level of a new (LP0) and used (LP1-LP6) AHRS in comparison with manufacturers value. The
829 noise height is calculated using the fit value to the real sensors.

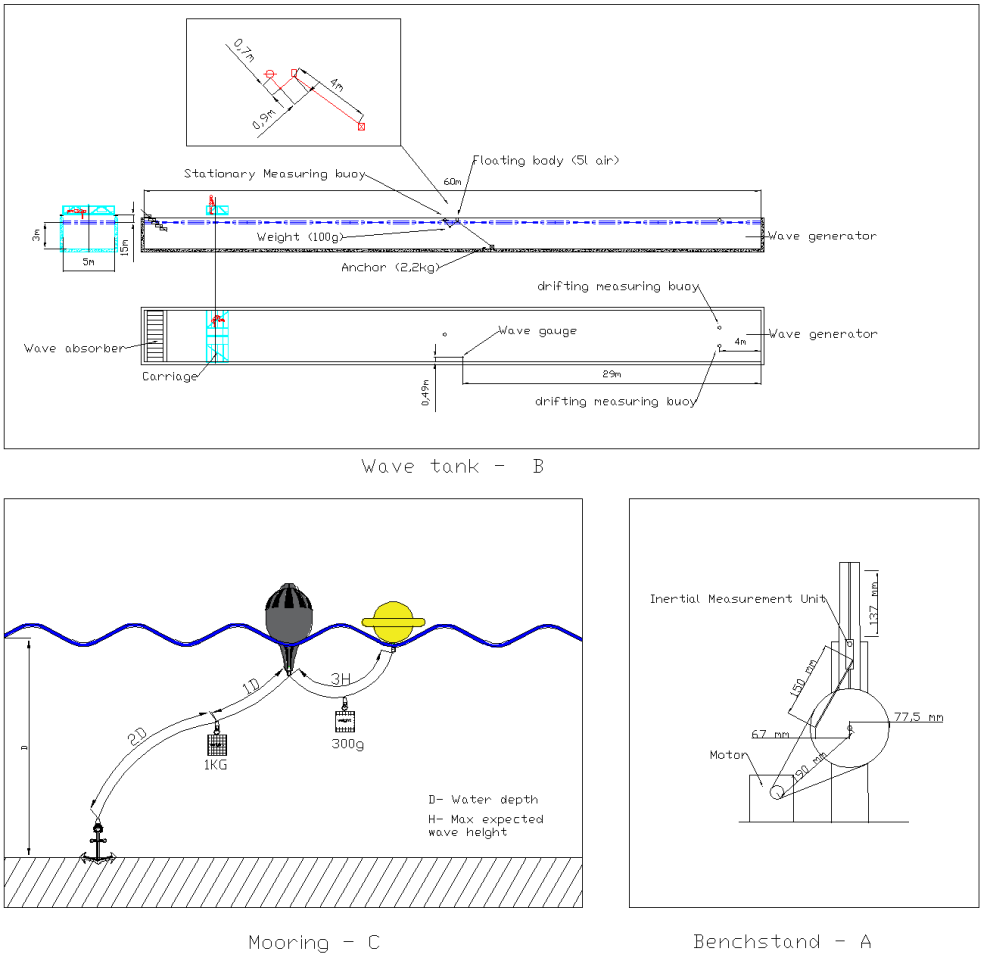

FIG. 4. Technical drawings of a) benchstand; b) wave tank and c) recommended mooring setup.

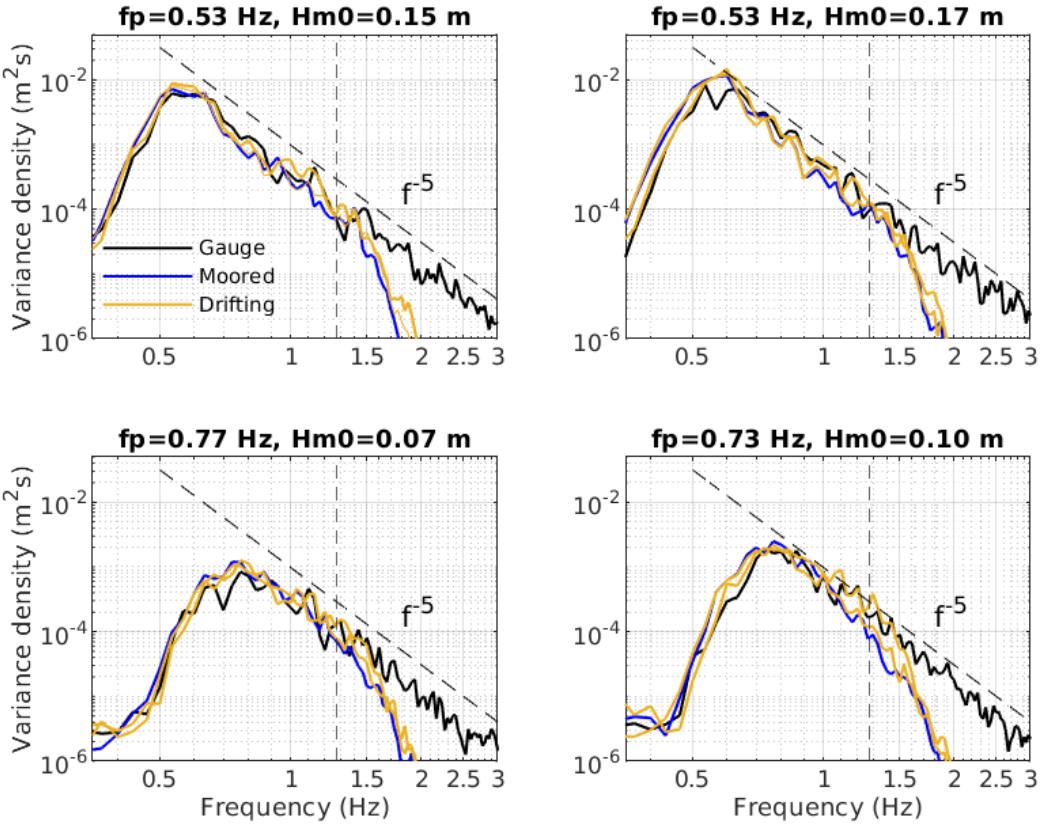

830 FIG. 5. Comparison of drifting and moored LP's with wave gauge at a wave tank. The wave field corresponds
831 to the JONSWAP spectrum. 1.28 Hz cut-off frequency is marked by a vertical dashed line.

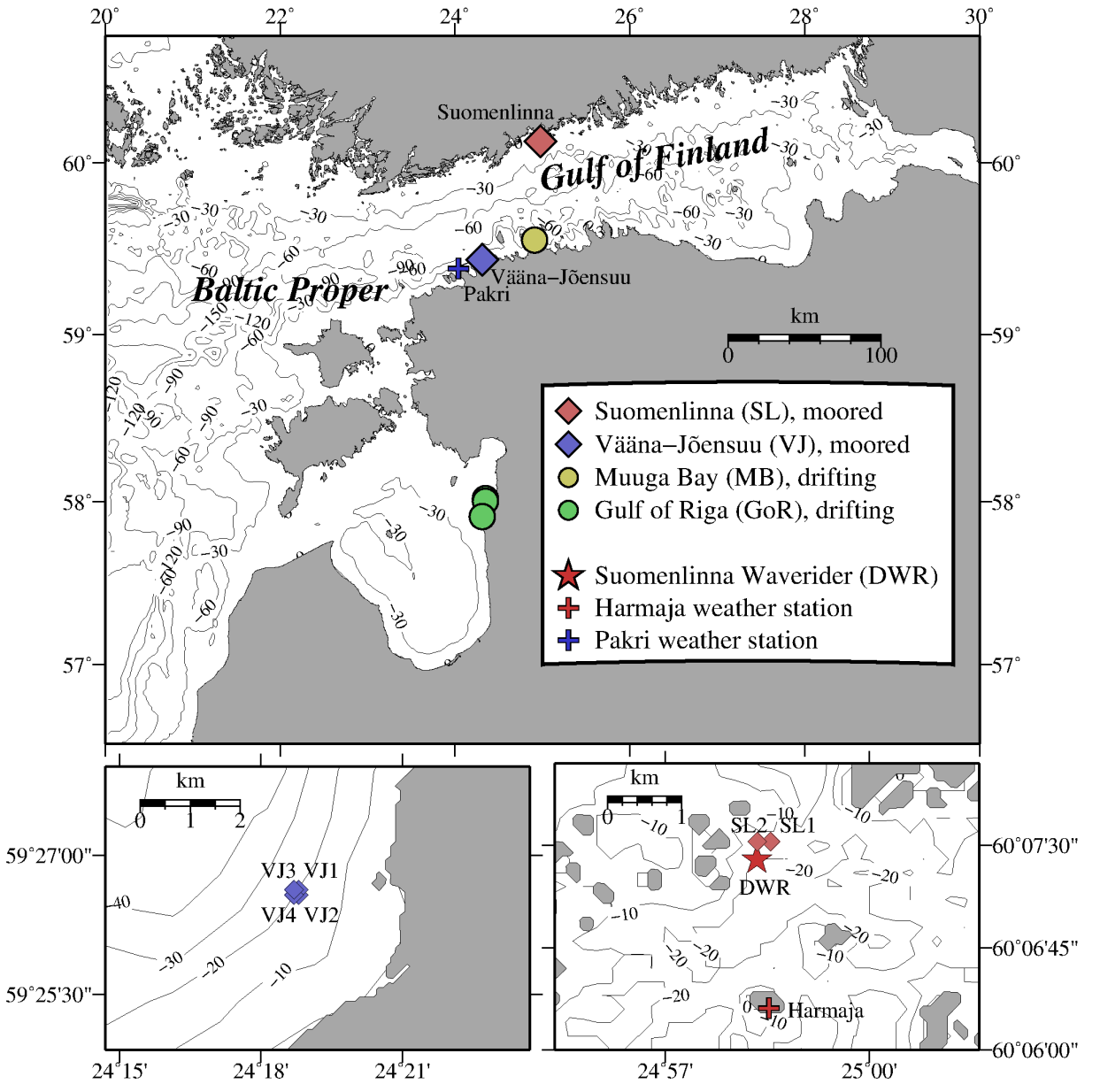

832 FIG. 6. Field test sites where LainePoiss's were moored (diamond) or deployed as drifters (circle). Existing
833 operational wave and wind measurements are shown with a star and plus-signs.

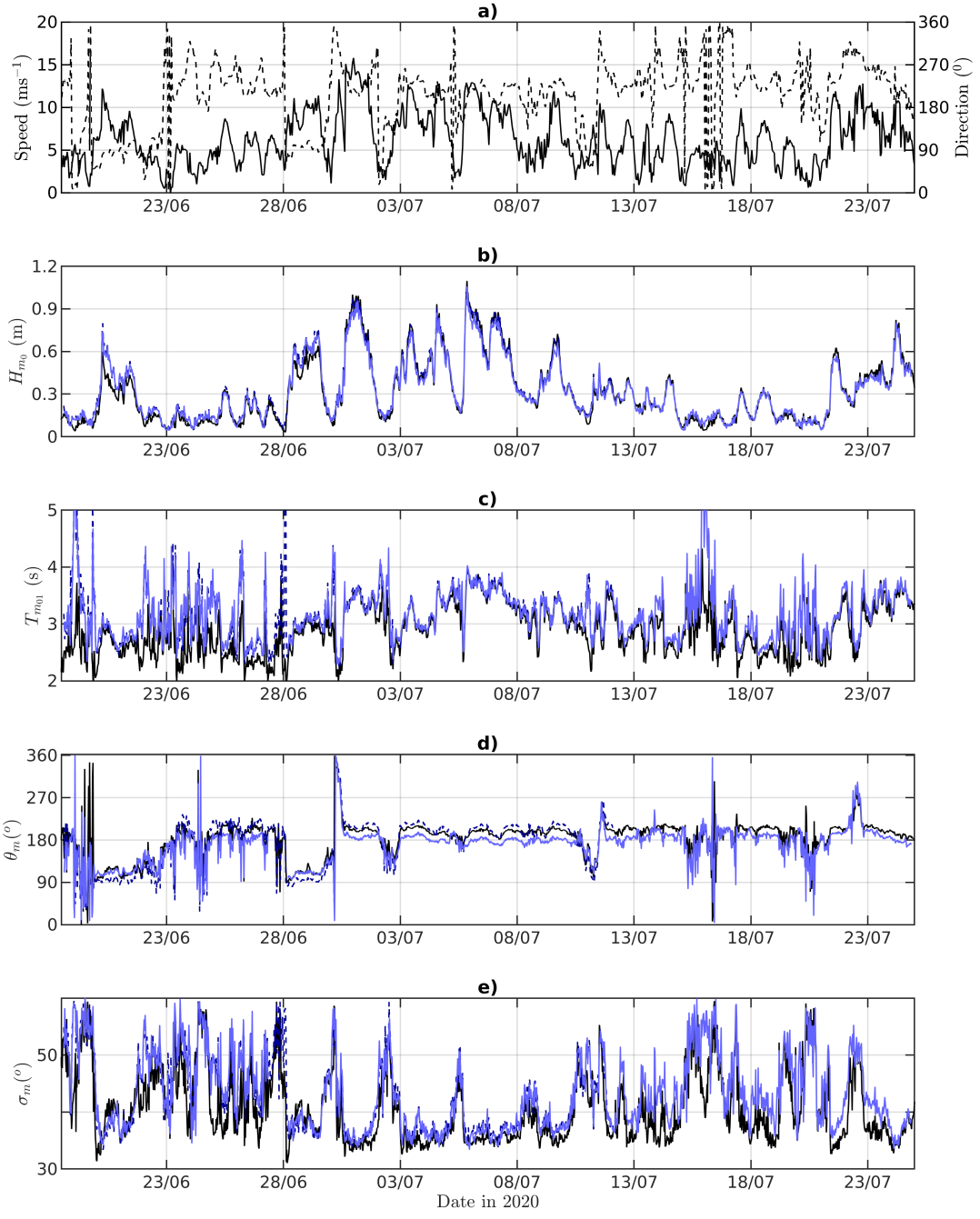

834 FIG. 7. Suomenlinna validation period 1. Black line on panel a) is wind speed and dashed black line wind
835 direction. Black line on panels b-e are DWR, blue ones LP.

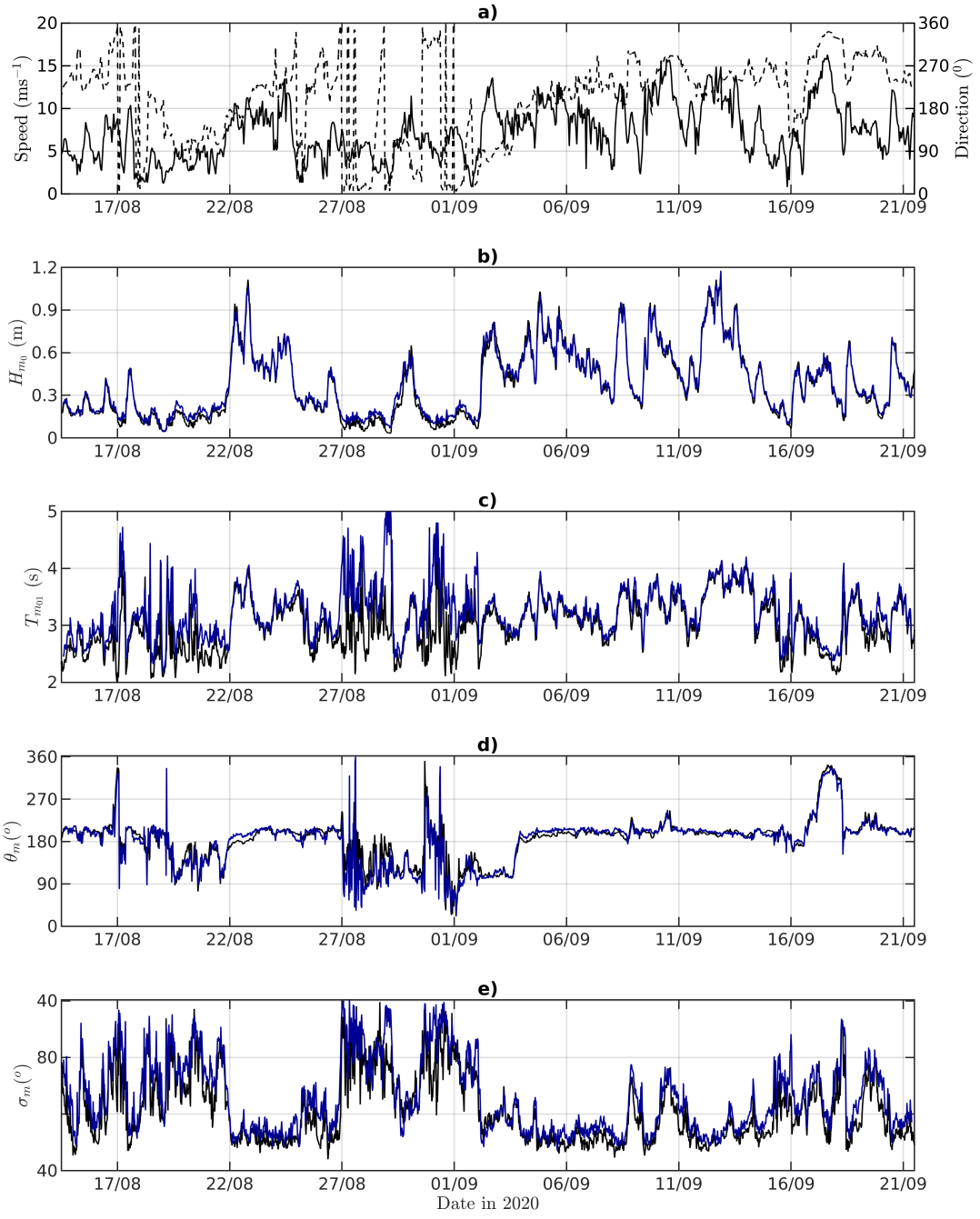

FIG. 8. Same as Fig. 7 but for second validation period.

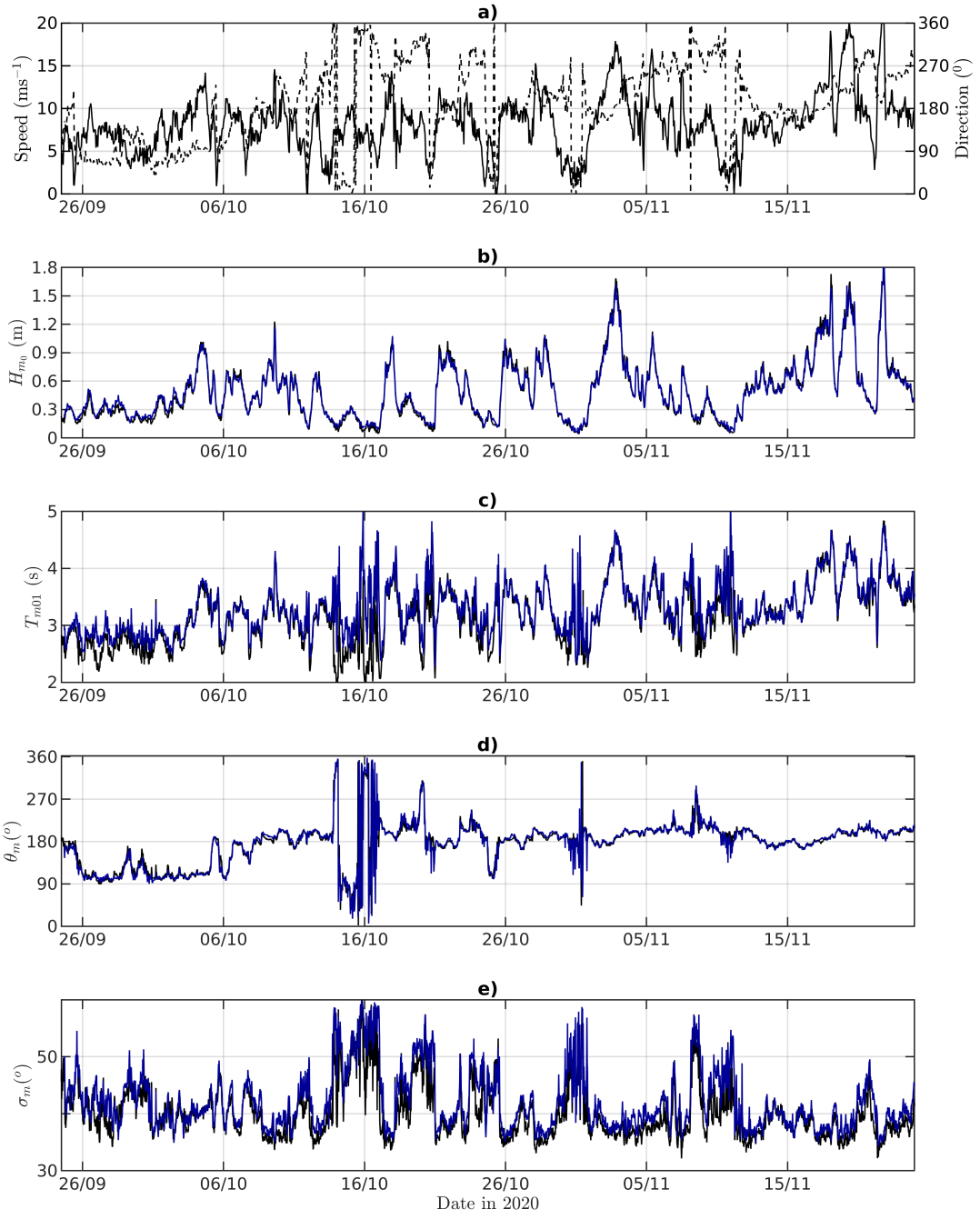

FIG. 9. Same as Fig. 7 but for third validation period.

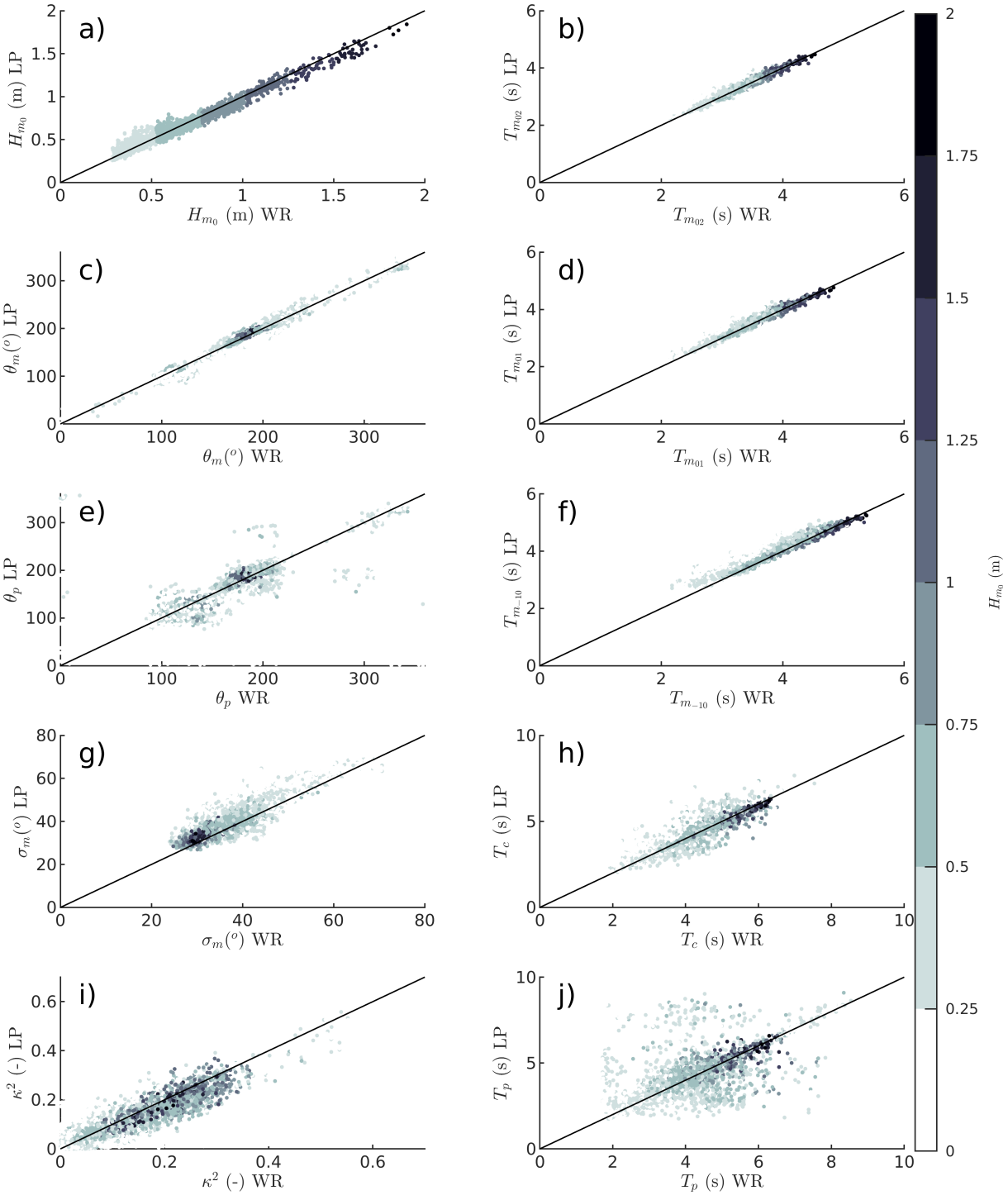

836 FIG. 10. Scatter plot of wave parameters during Suomenlinna validation deployment grouped by significant
837 wave height. For the definition of variables see Section 3.

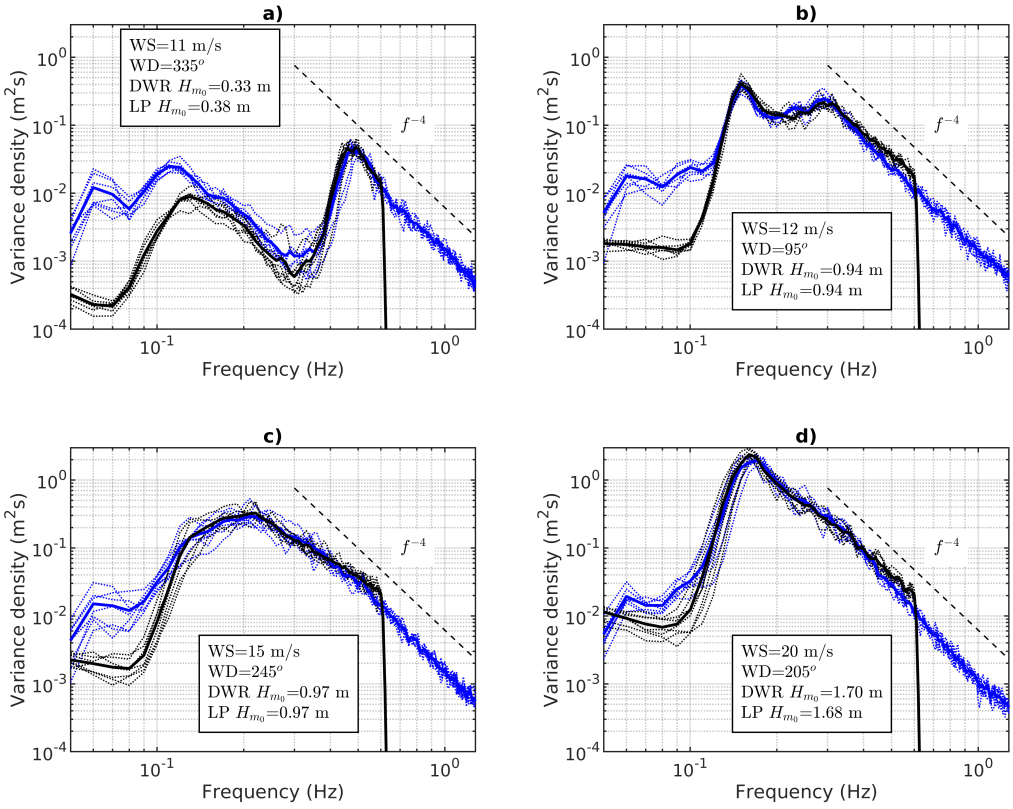

838 FIG. 11. Comparison of wave spectra at Suomenlinna for four different wind directions. Black lines are DWR,
839 blue lines are LP. The thin dotted lines correspond to 30 min spectra, while the thick lines are averaged spectra
840 of 7 individual spectra.

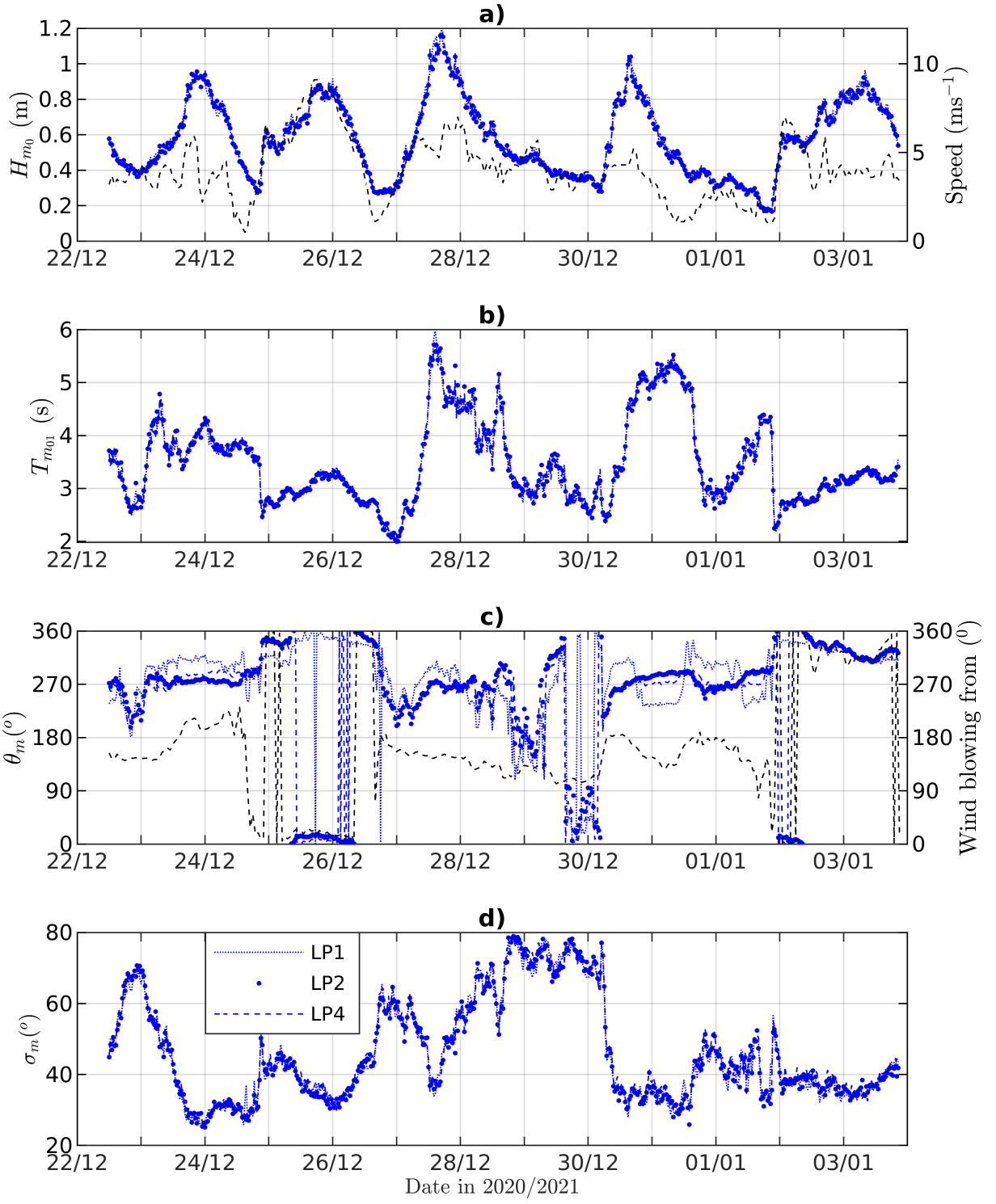

841 FIG. 12. Intercomparison of three LP's moored simultaneously about 100 m apart. On panel a) the dashed
842 black line marks the wind speed from Pakri weather station and on panel c) the wind direction.

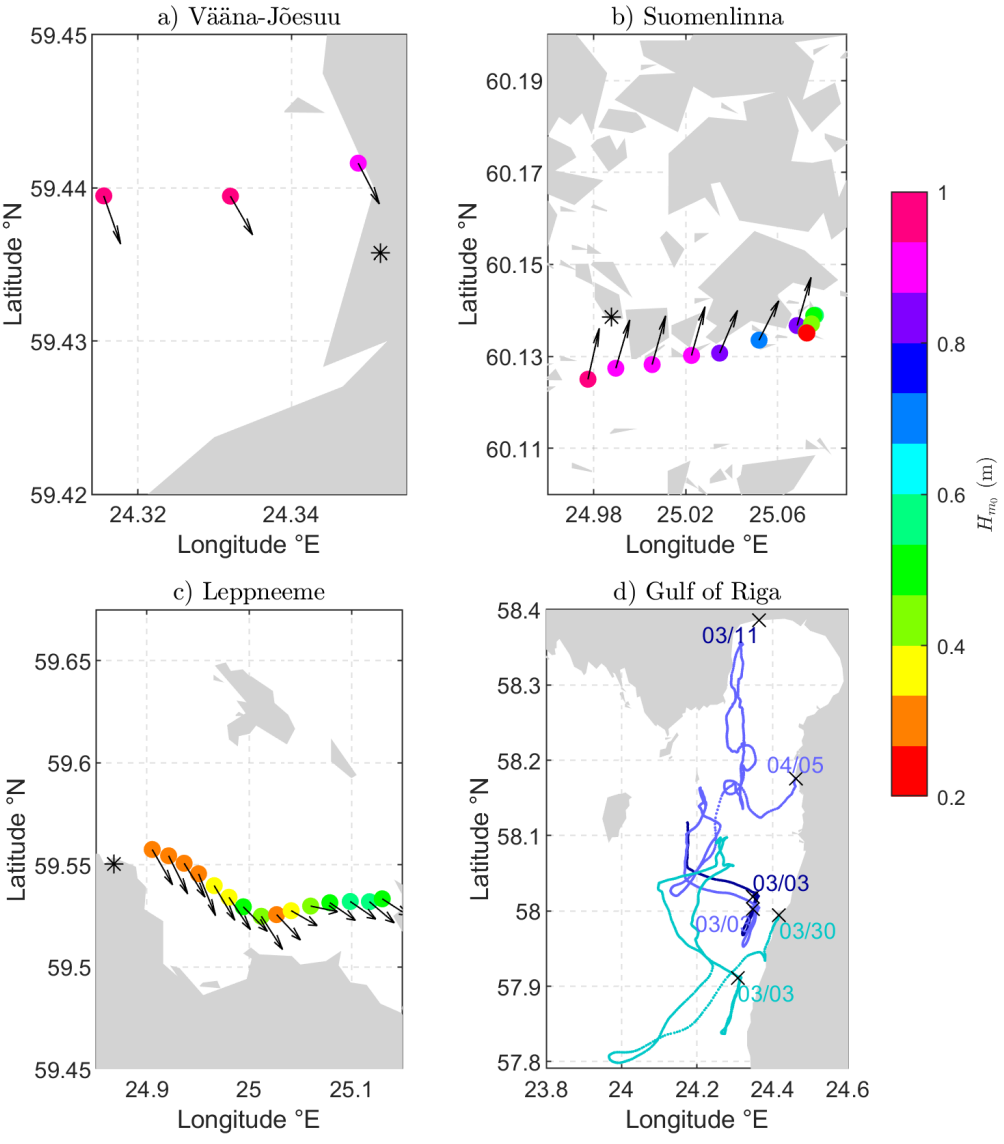

843 FIG. 13. Drifting experiments results. UAV ground stations are marked with asterisks. Panel d) only displays
844 tracks of buoys, because most of the time no wave motion in ice was present. Also on panel d), X marks the
845 deployment or retrieval locations. For the dates of the experiments, see Table 6.

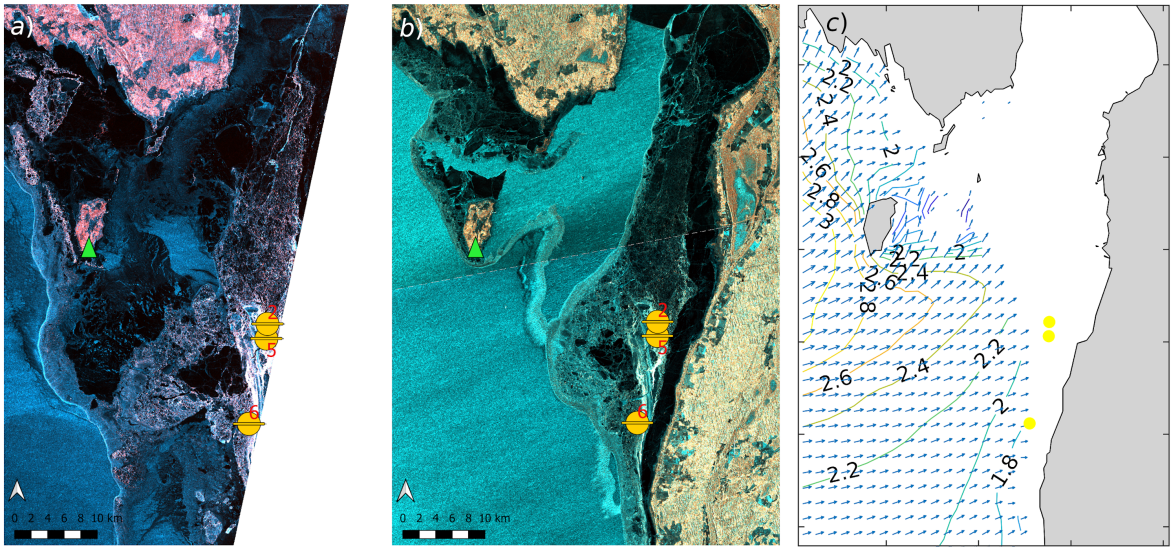

FIG. 14. a) SAR image at 04UTC; b) SAR image at 16UTC; c) CMEMS model wave field (Significant wave height, m; wave directions, arrows) at 16UTC. The locations of different LP's at 16UTC are shown with yellow marks. Kihnu weather station is marked with a green filled triangle. The times are for 06.03.2021.

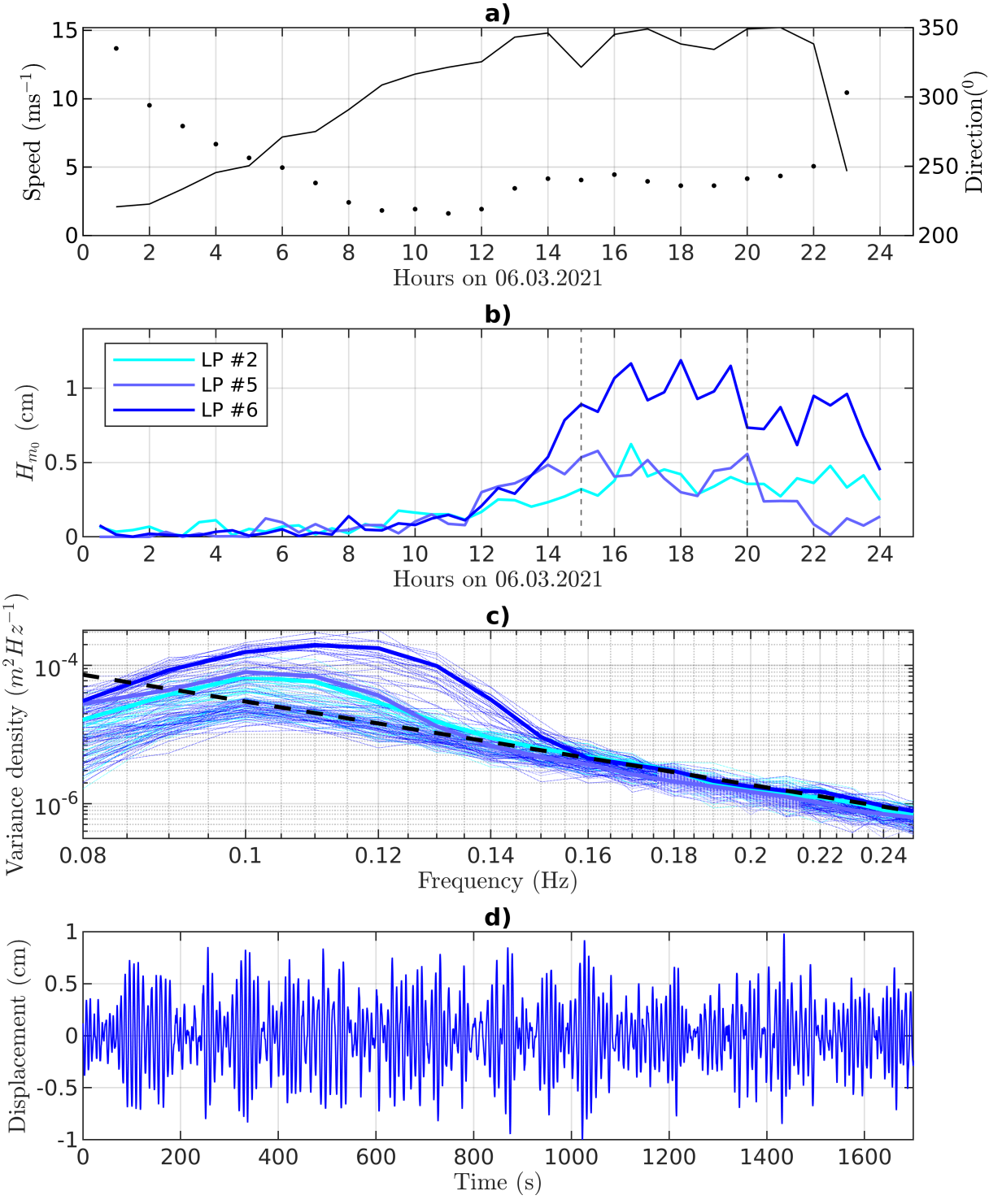

FIG. 15. Waves in ice measurements. a) wind speed and direction at Kihnu weather station (for location, see Fig. 14; direction marked with dots); b) Significant wave height from three buoys in ice; c) Spectra of three buoys with thin dotted lines corresponding to 30 min single spectra and thick lines corresponding to averaged spectra; dashed black line shows the sensor noise floor; d) Surface displacement for buoy #6 in ice.

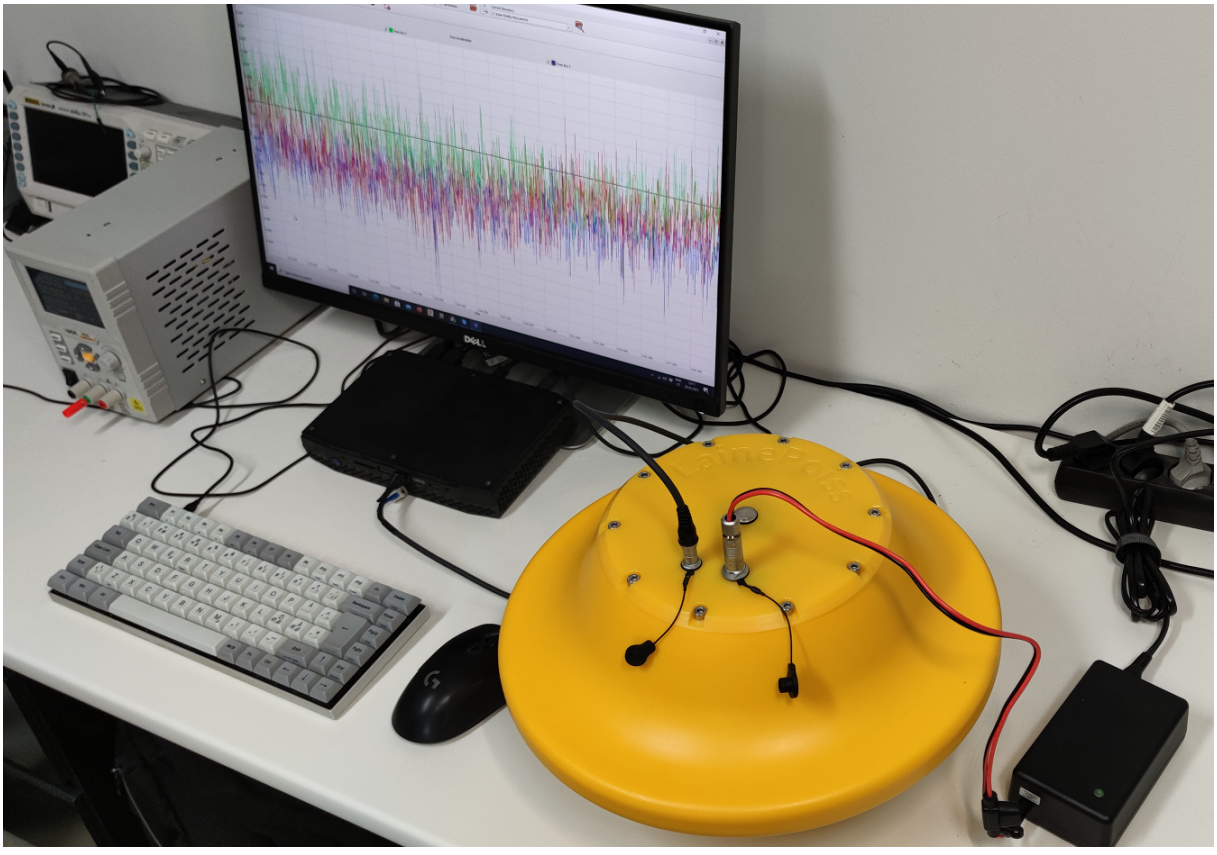

FIG. 16. New version of the buoy, with the charging and data acquisition connectors brought outside the buoy to reduce buoy openings.